

NF-κB–dependent IRF1 activation programs cDC1 dendritic cells to drive antitumor immunity

Ghita Ghislat, Ammar Cheema, Elodie Baudoin, Christophe Verthuy, Pedro Ballester, Karine Crozat, Noudjoud Attaf, Chuang Dong, Pierre Milpied, Bernard Malissen, et al.

▶ **To cite this version:**

Ghita Ghislat, Ammar Cheema, Elodie Baudoin, Christophe Verthuy, Pedro Ballester, et al.. NF-κB–dependent IRF1 activation programs cDC1 dendritic cells to drive antitumor immunity. Science Immunology, 2021, 6 (61), pp.eabg3570. 10.1126/sciimmunol.abg3570 . hal-03329415

HAL Id: hal-03329415
https://amu.hal.science/hal-03329415

Submitted on 16 May 2022

HAL is a multi-disciplinary open access archive for the deposit and dissemination of scientific research documents, whether they are published or not. The documents may come from teaching and research institutions in France or abroad, or from public or private research centers.

L'archive ouverte pluridisciplinaire **HAL**, est destinée au dépôt et à la diffusion de documents scientifiques de niveau recherche, publiés ou non, émanant des établissements d'enseignement et de recherche français ou étrangers, des laboratoires publics ou privés.

NF-κB–dependent IRF1 activation programs cDC1 dendritic cells to drive antitumor immunity

Ghita Ghislat[1], Ammar S. Cheema[1], Elodie Baudoin[1], Christophe Verthuy[1], Pedro J. Ballester[2], Karine Crozat[1], Noudjoud Attaf[1], Chuang Dong[1], Pierre Milpied[1], Bernard Malissen[1], Nathalie Auphan-Anezin[1], Thien P. Vu Manh[1], Marc Dalod[1†], Toby Lawrence[1,3,4*†]

Conventional type 1 dendritic cells (cDC1s) are critical for antitumor immunity. They acquire antigens from dying tumor cells and cross-present them to CD8⁺ T cells, promoting the expansion of tumor-specific cytotoxic T cells. However, the signaling pathways that govern the antitumor functions of cDC1s in immunogenic tumors are poorly understood. Using single-cell transcriptomics to examine the molecular pathways regulating intratumoral cDC1 maturation, we found nuclear factor κB (NF-κB) and interferon (IFN) pathways to be highly enriched in a subset of functionally mature cDC1s. We identified an NF-κB–dependent and IFN-γ–regulated gene network in cDC1s, including cytokines and chemokines specialized in the recruitment and activation of cytotoxic T cells. By mapping the trajectory of intratumoral cDC1 maturation, we demonstrated the dynamic reprogramming of tumor-infiltrating cDC1s by NF-κB and IFN signaling pathways. This maturation process was perturbed by specific inactivation of either NF-κB or IFN regulatory factor 1 (IRF1) in cDC1s, resulting in impaired expressi on of IFN-γ–responsive genes and consequently a failure to efficiently recruit and activate antitumoral CD8⁺ T cells. Last, we demonstrate the relevance of these findings to patients with melanoma, showing that activation of the NF-κB/IRF1 axis in association with cDC1s is linked with improved clinical outcome. The NF-κB/IRF1 axis in cDC1s may therefore represent an important focal point for the development of new diagnostic and therapeutic approaches to improve cancer immunotherapy.

INTRODUCTION

Immunotherapy has brought unprecedented advances in cancer treatment, yet still most patients do not respond to current therapies. Hence, there is a strong need to further understand what dictates patient responses to immunotherapy and design new approaches to improve therapeutic outcomes. Previous studies in several preclinical cancer models support an important contribution of conventional type 1 dendritic cells (cDC1s) to effective immunotherapy, including adoptive T cell therapy and immune checkpoint blockade (*1*–*3*). Furthermore, the frequency of cDC1s in human cancers is associated with improved prognosis and response to immunotherapy (*4*). cDC1s in humans and mice share development pathways and phenotypic markers, including expression of the chemokine receptor XCR1 as a lineage marker (*4*, *5*). The defining property of cDC1s is the cross-presentation of antigens via the class I major histocompatibility complex (MHC) pathway to CD8⁺ T cells (*6*), which is critical for antitumor immune responses (*7*). In line with this function, cDC1s express a number of molecules associated with the uptake and processing of antigens from dying cells for cross-presentation (*8*). However, cross-presentation alone is not sufficient for the cDC1-dependent control of tumor growth (*9*), implying that other functions of cDC1s play important roles in antitumor immunity. For example, DCs can be important sources of chemokines and cytokines that promote CD8⁺ T cell recruitment and activation in tumors. However, the tumor microenvironment suppresses the recruitment and activation of cDC1s, through various mechanisms, which contributes to evasion of antitumor immunity and may underlie resistance to immunotherapy in patients with cancer (*4*). The intrinsic molecular pathways regulating intratumoral cDC1 functions remain poorly understood but are critical to determining how cDC1s can be targeted to improve cancer immunotherapy.

Previous studies have been hampered by the lack of experimental tools to dissect the specific functions of cDC1s, mostly relying on the use of Batf3-deficient mice that lack cDC1s, which precludes the study of pathways regulating cDC1 functions within tumors. The recent development of transgenic mice allowing the specific targeting of cDC1s, based on their specific expression of the chemokine receptor XCR1 (*4*, *5*), has revealed important new aspects of cDC1 functions in tumors. For example, targeted deletion of MHCII in Xcr1-expressing cells revealed an unexpected role in priming CD4⁺ T cells, which was required for rejection of transplanted tumors bearing a xenoantigen (*10*). Several reports have described the importance of cDC1s in various preclinical models for effective immunotherapy, including adoptive T cell therapy (*1*, *2*) and immune checkpoint blockade (*3*, *11*–*15*). In the context of adoptive T cell therapy, tumor-resident cDC1s were reported to produce the CXCR3-dependent chemokines CXCL9 and CXCL10, required for the recruitment of effector CD8⁺ T cells (*1*). In another study, increased interferon-γ (IFN-γ) production during anti–programmed cell death 1 (PD-1) therapy was shown to drive interleukin-12 (IL-12) expression by DCs, leading to increased CD8⁺ T cell activation (*16*). These studies demonstrated the important contribution of cDC1s to antitumor immune responses in the presence of activated CD8⁺ T cells producing IFN-γ.

[1]CNRS, INSERM, Centre d'Immunologie de Marseille-Luminy (CIML), Tu ring Center for Living Systems, Aix-Marseille University, 13009 Marseille, France. [2]Cancer Research Center of Marseille CRCM, INSERM, Institut Paoli-Calmettes, Aix-Marseille University, CNRS, 13009 Marseille, France. [3]Centre for Inflammation Biology and Cancer Immunology, Cancer Research UK King's Health Partners Centre, School of Immunology and Microbial Sciences, King's College London, London SE1 1UL, UK. [4]Henan Key Laboratory of Immunology and Targeted Therapy, School of Laboratory Medicine, Xinxiang Medical University, Xinxiang, China.
*Corresponding author. Email: toby.lawrence@kcl.ac.uk
†These authors jointly supervised these studies.

Tumor immunogenicity and the recruitment of tumor-infiltrating CD8$^+$ T cells are critical factors for clinical responses to immunotherapy (*17*–*19*). Tumor antigens broadly fall into two categories: those specifically expressed by cancer cells, including neoantigens generated by genetic alterations, and those that are highly but not exclusively expressed by cancer cells. Neoantigens, associated with cancers with high mutational burden, exert the strongest T cell–mediated antitumor immunity, which often correlates with improved responses to immunotherapy (*20*). However, the roles of cDC1s in relation to intrinsic tumor immunogenicity have not yet been addressed. Here, we investigated the molecular pathways in tumor-infiltrating cDC1s that govern their antitumor functions in relation to tumor immunogenicity. Using genetic tools to specifically target cDC1s, we demonstrate their specific role in the control of immunogenic tumor growth. Single-cell RNA sequencing (scRNA-seq) revealed the trajectory of intratumoral cDC1 maturation and identified distinct activation states associated with tumor immunogenicity. By targeting specific signaling pathways in cDC1s, we identify molecular pathways that drive intratumoral cDC1 maturation leading to the recruitment and activation of antitumoral CD8$^+$ T cells. Last, we show that activation of these pathways in human melanoma correlates with a better clinical prognosis. Therefore, manipulating these pathways could offer new therapeutic strategies to overcome resistance to immunotherapy and improve outcomes for cancer treatment.

RESULTS

cDC1s are required for control of immunogenic tumors

To explore the role of cDC1s in relation to tumor immunogenicity, we used a clinically relevant mouse melanoma model based on expression of Braf^{V600E} and deletion of tumor suppressors *Pten* and *Cdkn2a*, specifically in melanocytes (YUMM1.7) (*21*, *22*). Previous studies have established that YUMM1.7 tumors are not immunogenic and do not show increased growth in Rag-deficient mice, which lack T and B lymphocytes (*21*). Consequently, these tumors are also resistant to immune checkpoint therapy. We exploited the fact that YUMM1.7 tumors derived from male mice express the minor histocompatibility antigen H-Y (*23*) to assess tumor growth in an allogeneic setting by transplanting YUMM1.7 tumors in syngeneic female mice. Although tumors progressed in both male and female mice, tumor growth rate was significantly reduced in females (Fig. 1A), which was associated with a strong increase in leukocyte infiltration (fig. S1A), suggesting that YUMM1.7 tumors were immunogenic in female mice. Analysis of tumor-infiltrating CD8$^+$ T cells showed a substantial increase in recruitment of effector CD8$^+$ T cells expressing IFN-γ and tumor necrosis factor–α (TNF-α) in tumors from female mice compared with males (Fig. 1B). In addition, analysis of gene expression in tumor-infiltrating CD8$^+$ T cells from female mice revealed increased expression of genes underpinning effector functions (fig. S1B) (*21*, *22*). Analysis of cytokines in tumor lysates also showed an increased production of various chemokines and inflammatory cytokines in tumors from female mice compared with males (fig. S1, C and D). To confirm the specificity of the T cell response in female mice, we next assessed the frequency of CD8$^+$ T cells recognizing the tumor-associated H-Y antigen, by using MHCI tetramers. As expected, H-Y–specific CD8$^+$ T cells were absent from YUMM1.7 tumors in male mice but were readily detected in tumors from females (Fig. 1C). These data established the intrinsic immunogenicity of YUMM1.7 tumors in female mice.

Taking advantage of the difference in immunogenicity between YUMM1.7 tumors in male and female mice, we proceeded to evaluate the specific contribution of cDC1s to the control of tumor growth. Previous studies implicating cDC1s in antitumor immune responses and immunotherapy in preclinical models had used *Batf3*-deficient mice constitutively lacking cDC1s. However, Batf3 is not exclusively expressed by cDC1s, and these mice display other phenotypes, including intrinsic defects in memory CD8$^+$ T cells (*24*, *25*), reduced numbers of cDC2s (*14*), and an increased frequency of regulatory T cells (*26*). In contrast, the chemokine receptor XCR1 is a specific marker for cDC1s conserved in humans and mice (*4*, *5*). Thus, we used mutant mice expressing the active diphtheria toxin receptor subunit [diphtheria toxin A (DTA)] exclusively in *Xcr1*-expressing cells to examine the specific role of cDC1s in control of tumor growth. These mice were generated by crossing the *Xcr1*^{iCre} knock-in mice (*26*, *27*) with mice expressing DTA from the ubiquitous *Rosa26* locus under control of a lox-STOP-lox cassette (*R26*$^{lsl\text{-}DTA}$) (*28*). YUMM1.7 tumors were transplanted into cohorts of male and female *Xcr1*^{iCre};*R26*$^{lsl\text{-}DTA}$ mice (*Xcr1*^{DTA}) or DTA-negative littermate controls [*R26*$^{lsl\text{-}DTA}$ or *Xcr1*^{iCre} mice; wild-type (WT)]. Flow cytometry analysis confirmed that tumor-associated cDC1s were almost completely absent in *Xcr1*^{DTA} mice, compared with WT controls (Fig. 1, D and E). We observed a consistent increase in MHCII$^+$CD-11c^{hi} cells in tumors from *Xcr1*^{DTA} mice, most of which appeared to represent cDC2s (fig. S1, E and F). There was also an inconsistent increase in MHCII$^+$CD11c$^-$ cells, which appeared to represent tumor-infiltrating monocytes (fig. S1G).

The kinetics of YUMM1.7 tumor growth was unaffected in both WT and *Xcr1*^{DTA} male mice. However, tumor growth was significantly increased in female *Xcr1*^{DTA} mice compared with WT controls (Fig. 1, F and G). Thus, Xcr1$^+$ cDC1s were required for control of immunogenic tumors. Increased tumor growth upon depletion of cDC1s in female mice was associated with a drastic decrease in the recruitment of tumor-infiltrating CD8$^+$ T cells (Fig. 1H). Depletion of cDC1s also significantly reduced the frequency of tumor (H-Y)–specific CD8$^+$ T cells in YUMM1.7 tumors from female mice (Fig. 1I and fig. S1H), and the accumulation of IFN-γ– and granzyme B (GrB)–expressing cytotoxic CD8$^+$ T cells (CTLs) (Fig. 1J). Despite the efficient depletion of cDC1s in tumor-draining lymph nodes (TDLNs) (fig. S1I), the frequency of H-Y–specific CD8$^+$ T cells and CTLs in TDLNs was unaffected (fig. S1, J and K). We did not observe an increase in the frequency of H-Y tetramer$^+$ CD8$^+$ T cells in TDLNs of WT female mice bearing YUMM1.7 tumors at any time point from day 10 onward (fig. S1L), suggesting that cDC1-mediated activation of tumor-infiltrating CD8$^+$ T cells occurs locally at the tumor site, rather than in TDLNs by migratory DCs.

To rule out the potential effects of sexual dimorphism on differences in YUMM1.7 tumor growth, we used an immunogenic YUMM1.7 tumor line derived from ultraviolet-irradiated male tumor-bearing mice (YUMMER1.7) (*22*). These tumors exhibit a high somatic mutational burden and, unlike YUMM1.7, their growth was significantly decreased in immunocompetent male mice as compared with immunodeficient mice (*22*), presumably because of increased expression of neoantigens. As expected, YUMMER1.7 tumors spontaneously regressed in syngeneic male WT mice (Fig. 1, K and L), which was associated with the accumulation of IFN-γ– and TNF-α–expressing CD8$^+$ T cells in TDLNs (Fig. 1M). However, male *Xcr1*^{DTA} mice completely failed to control the growth of YUMMER1.7 tumors (Fig. 1, N and O), which was accompanied by a reduced

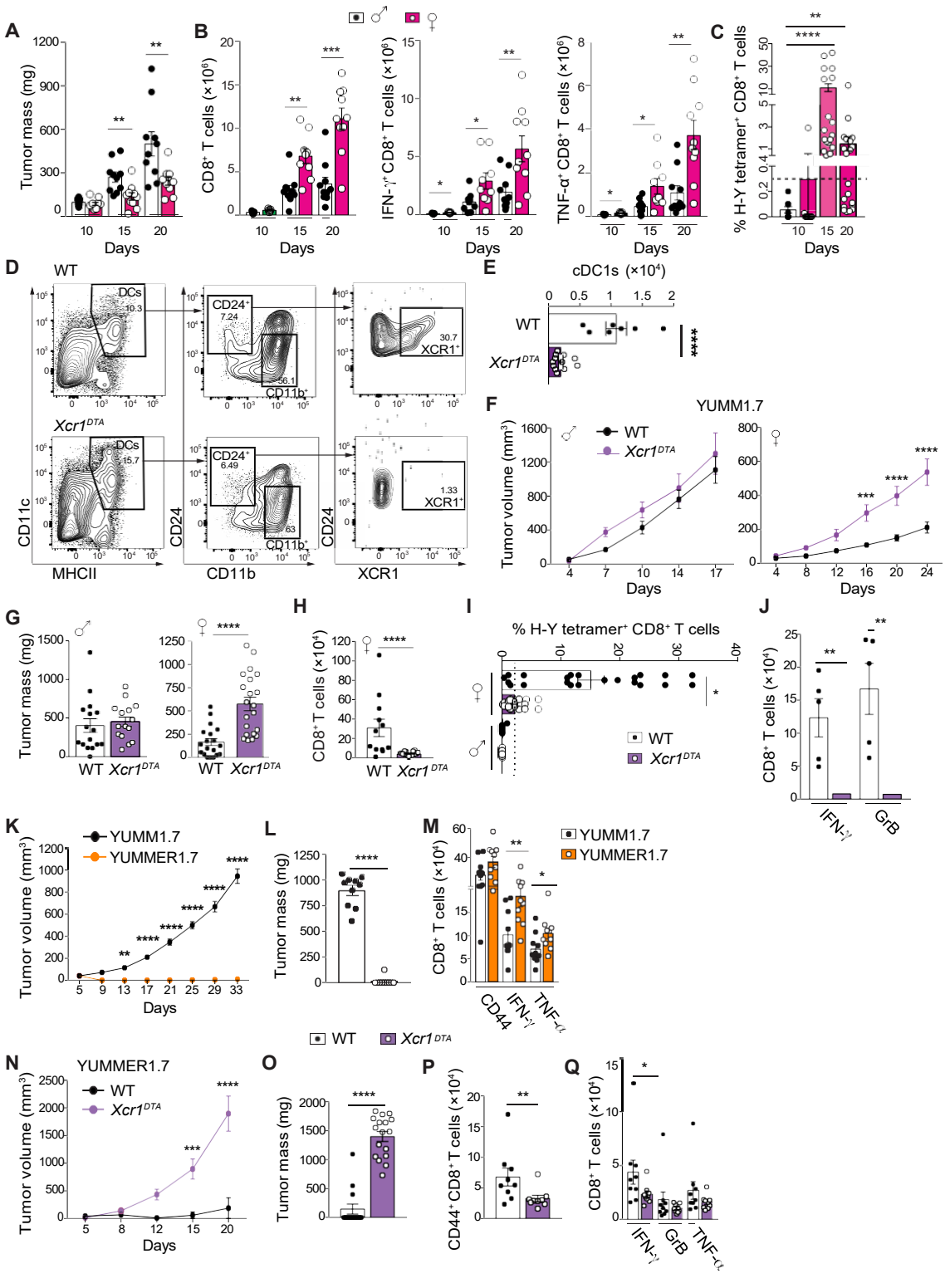


Fig. 1. cDC1s are required for control of immunogenic tumor growth. (**A**) YUMM1.7 tumor growth in male and female mice. (**B**) Quantification of tumor-infiltrating $CD8^+$ T cells, and IFN-γ, or TNF-α–producing $CD8^+$ T cells, by flow cytometry in YUMM1.7 tumors from male and female mice at end point. (**C**) Tetramer analysis of H-Y–specific $CD8^+$ T cells ($Smcy_{(738–746)}$/H-$2D^b$ and $Uty_{(243–254)}$/H-$2D^b$) in YUMM1.7 tumors. The dashed line represents the highest frequency obtained with an irrelevant control epitope (HPV16 $E7_{(49–57)}$/H-$2D^b$). (**D**) Representative flow cytometry analysis of cDC1s in YUMM1.7 tumors (gated in $CD3^-$ $CD19^-$ $NK1.1^-$ $Ly6G^-$ $CD11c^+$ $MHCII^+$ $CD64^-$ cells) from female WT and *Xcr1*^{DTA} mice. (**E**) Total number of cDC1s from female WT and *Xcr1*^{DTA} mice bearing YUMM1.7 tumors. Graphs represent pooled data from two independent experiments. (**F** and **G**) YUMM1.7 tumor growth in male and female WT or *Xcr1*^{DTA} mice. (**H** to **J**) Quantification of total $CD8^+$ T cells (H), frequency of H-Y $tetramer^+$ $CD8^+$ T cells (I), and IFN-γ– or GrB–producing $CD8^+$ T cells (J) in YUMM1.7 tumors from WT and *Xcr1*^{DTA} mice at end point. (**K** and **L**) Growth of YUMM1.7 and YUMMER1.7 tumors in male mice. (**M**) Quantification of $CD44^+$ $CD8^+$ T cells and IFN-γ– or TNF-α–producing cells at end point in TDLNs from mice engrafted with YUMM1.7 or YUMMER1.7 tumors. (**N** and **O**) YUMMER1.7 tumor growth in male WT and *Xcr1*^{DTA} mice. (**P** and **Q**) Quantification of $CD44^+$ $CD8^+$ T cells (P) and IFN-γ–, GrB–, or TNF-α–producing cells (Q) at end point in TDLN from mice engrafted with YUMMER1.7 tumors. Total cell numbers are indicated for 250 mg of tumor tissue. Pooled data or representative data from at least two independent experiments are shown. Data are represented as means ± SEM of $n = 5$ to 10 mice. In scatter plots, each point corresponds to an individual mouse. Statistical analysis was performed by two-way ANOVA followed by Sidak's multiple comparison test (F, K, and N) or Mann-Whitney test. Fisher's exact test was used for the frequency of $tetramer^+$ cells when their proportion was above the highest level obtained with HPV16 $E7_{(49–57)}$/H-$2D^b$ tetramer (C and I).

accumulation of activated CD8+ T cells in TDLNs (Fig. 1, P and Q), but not in nondraining LNs (fig. S1M). These experiments demonstrated the specific contribution of cDC1s to the recruitment and activation of effector T cells and the control of immunogenic tumor growth.

Defining the molecular determinants of cDC1 maturation in tumors

The molecular pathways that control the activation and functions of tumor-infiltrating cDC1s remain largely unknown. To reveal the molecular determinants of intratumoral cDC1 maturation during control of immunogenic tumor growth, we performed scRNA-seq of cDC1s isolated from YUMM1.7 tumors in female mice. Considering the scarcity of cDC1s in tumors, we used an index cell sorting approach that enabled us to track the cell surface phenotype of single cells and their transcriptomes. We used a flow cytometry–based 5′-end scRNA-seq method termed FB5P-seq (*29*), which enables the sequencing of phenotypically defined single cells and incorporates unique molecular identifiers (UMIs) for accurate molecular counting. After quality control and contaminant filtering, we obtained single-cell transcriptomes from 113 bona fide cDC1s (gated on CD3− CD19− NK1.1− Ly6G− CD11c+ MHCII+ CD64− cells). Unsupervised clustering analysis using Seurat (*27*) revealed substantial heterogeneity among intratumoral cDC1s, with four clusters (C0 to C3) visualized by Uniform Manifold Approximation and Projection (UMAP) and expressing highly distinct gene signatures (GSs) (Fig. 2A and fig. S2A). Gene set enrichment analysis (GSEA) across the four clusters, combining gene sets from the MsigDB public repository and previously published DC GSs, revealed enrichment for distinct biological functions and activation states (Fig. 2B). C3 was enriched for signatures associated with cell proliferation (E2F targets, G2M checkpoint, and DNA replication) and an immature state [Core DN Vu Manh (*29*) and Mat OFF Ardouin (Fig. 2, B and D) (*31*)]. Core DN Vu Manh corresponds to gene sets down-regulated across human and mouse DC subsets during maturation in response to microbial stimuli (*29*). Mat OFF Ardouin corresponds to gene sets down-regulated during steady-state maturation of mouse cDC1s (*32*). C0 also showed enrichment of signatures from immature cDC1s. Conversely, C1 showed a high enrichment for genes up-regulated in mature cDC1s [Core UP Vu Manh (*29*) and Mat ON Ardouin (*30*)]. In addition, genes associated with nuclear factor κB (NF-κB) and IFN signaling pathways were enriched in C1. EnrichR analyses using Kyoto Encyclopedia of Genes and Genomes (KEGG), Reactome, and Protein-Protein Interaction (PPI) databases also revealed an enrichment for the NF-κB pathway in C1 (fig. S2B). Accordingly, the typical DC maturation markers *Ccr7*, *Cd40*, and *Fscn1* as well as the proinflammatory cytokines *Il12b*, *Ccl5*, *Cxcl9*, and *Ccl22*, which are known target genes for the NF-κB pathway in DCs (*30*), were highly expressed in C1 (Fig. 2C). These data suggested that NF-κB signaling could be a key regulator of intratumoral cDC1 maturation, which prompted us to further explore the specific role of NF-κB in cDC1s.

NF-κB controls IFN-γ–mediated programming of cDC1s in tumors

To explore the role of NF-κB activation in cDC1s, we generated mice with a conditional deletion of IκB (inhibitor of NF-κB) kinase β (IKKβ) (*Ikbkb* gene), a critical kinase for NF-κB activation, specifically in cDC1s. We crossed $Xcr1^{iCre}$ mice with $Ikbkb^{F/F}$ mice and confirmed efficient deletion of IKKβ specifically in cDC1s in homozygous $Ikbkb^{F/F}$ $Xcr1^{iCre/+}$ progeny ($Ikbkb^{\Delta Xcr1}$), at both mRNA and protein levels (fig. S3, A to F). There were no signs of autoimmunity or dysregulated immune homeostasis in $Ikbkb^{\Delta Xcr1}$ mice (fig. S3, G to I), unlike previous observations in mice lacking IKKβ throughout the DC lineage ($Ikbkb^{\Delta Itgax}$ mice) (*30*). This indicated that IKKβ/NF-κB activation in cDC1s was not required for tolerance and immune homeostasis, which implies that the phenotype observed in $Ikbkb^{\Delta Itgax}$ mice was likely due to IKKβ/NF-κB signaling in cDC2s, as previously suggested (*30*). However, $Ikbkb^{\Delta Xcr1}$ mice did present a partial defect in steady-state migratory cDC1s in skin-draining LNs (fig. S3, J to O), confirming that IKKβ/NF-κB signaling regulates steady-state cDC1 maturation. We did not observe the same increase in CD11chi cDC2s in $Ikbkb^{\Delta Xcr1}$ mice (fig. S3P), as seen in $Xcr1^{DTA}$ mice (fig. S1, E and F).

We next transplanted YUMM1.7 tumors in cohorts of male and female $Ikbkb^{\Delta Xcr1}$ mice and littermate controls. IKKβ deletion in cDC1s had no impact on tumor growth in male mice (fig. S4, A and B). However, YUMM1.7 tumor growth was significantly increased in female $Ikbkb^{\Delta Xcr1}$ mice compared with littermate controls (Fig. 3A). In addition, male $Ikbkb^{\Delta Xcr1}$ mice failed to control the growth of YUMMER1.7 tumors (Fig. 3B). These results demonstrated that IKKβ was required in cDC1s for control of immunogenic tumor growth. IKKβ deletion did not affect accumulation of cDC1s in tumors (fig. S4C) but reduced their expression of maturation markers including CD40, CD86, and CCR7 (although, in the case of CD86 and CCR7, this did not reach statistical significance); furthermore, CXCL9 expression by cDC1s in tumors from $Ikbkb^{\Delta Xcr1}$ mice was significantly reduced (Fig. 3, C and D). Conversely, IKKβ deletion in cDC1s did not affect the phenotype of tumor-associated cDC2s (Fig. 3, E and F), demonstrating that cell-intrinsic NF-κB signaling was required for maturation specifically of tumor-associated cDC1s. Similarly to $Xcr1^{DTA}$ mice, female $Ikbkb^{\Delta Xcr1}$ mice showed a strong decrease in the recruitment and activation of CD8+ T cells in YUMM1.7 tumors (Fig. 3, G and H, and fig. S4, D and E). Furthermore, the frequency of H-Y–specific CD8+ T cells was significantly reduced in tumors from these mice (Fig. 3I and fig. S4F), in line with data from $Xcr1^{DTA}$ mice. The impaired activation state of tumor-infiltrating CD8+ T cells in $Ikbkb^{\Delta Xcr1}$ mice was confirmed by gene expression analysis showing reduced expression of several T cell activation markers (Fig. 3J). In male $Ikbkb^{\Delta Xcr1}$ mice transplanted with YUMMER1.7 tumors, increased tumor growth was also associated with reduced expression of maturation markers by cDC1s (fig. S4G) and decreased accumulation of activated CD8+ T cells in TDLNs (Fig. 3, K and L), but not in nondraining LNs (fig. S4H). Collectively, these data demonstrated that NF-κB activation in intratumoral cDC1s was required for the recruitment and activation of CD8+ T cells and control of immunogenic tumors.

To gain further insight into the molecular mechanisms by which NF-κB drives cDC1-mediated control of tumor growth, we performed bulk RNA-seq analysis of cDC1s sorted from YUMM1.7 tumors in female $Ikbkb^{F/F}$ and $Ikbkb^{\Delta Xcr1}$ mice. GSEA revealed that IFN pathway GSs were highly enriched in WT cDC1s ($Ikbkb^{F/F}$) compared with IKKβ-deficient cells ($Ikbkb^{\Delta Xcr1}$) (Fig. 4A), with a particularly strong enrichment for the Interferon_gamma_response pathway (Fig. 4B). As expected, the TNFA_signaling_via_NF-κB pathway was also strongly enriched in WT cells, confirming an impaired activation of NF-κB after IKKβ deletion (Fig. 4A). To confirm changes in the IFN-γ response program in intratumoral cDC1s, we measured by quantitative reverse transcription polymerase chain reaction (qRT-PCR) the expression levels of hallmark genes induced by IFN-γ (*32*). IKKβ deletion in cDC1s led to a consistent down-regulation of

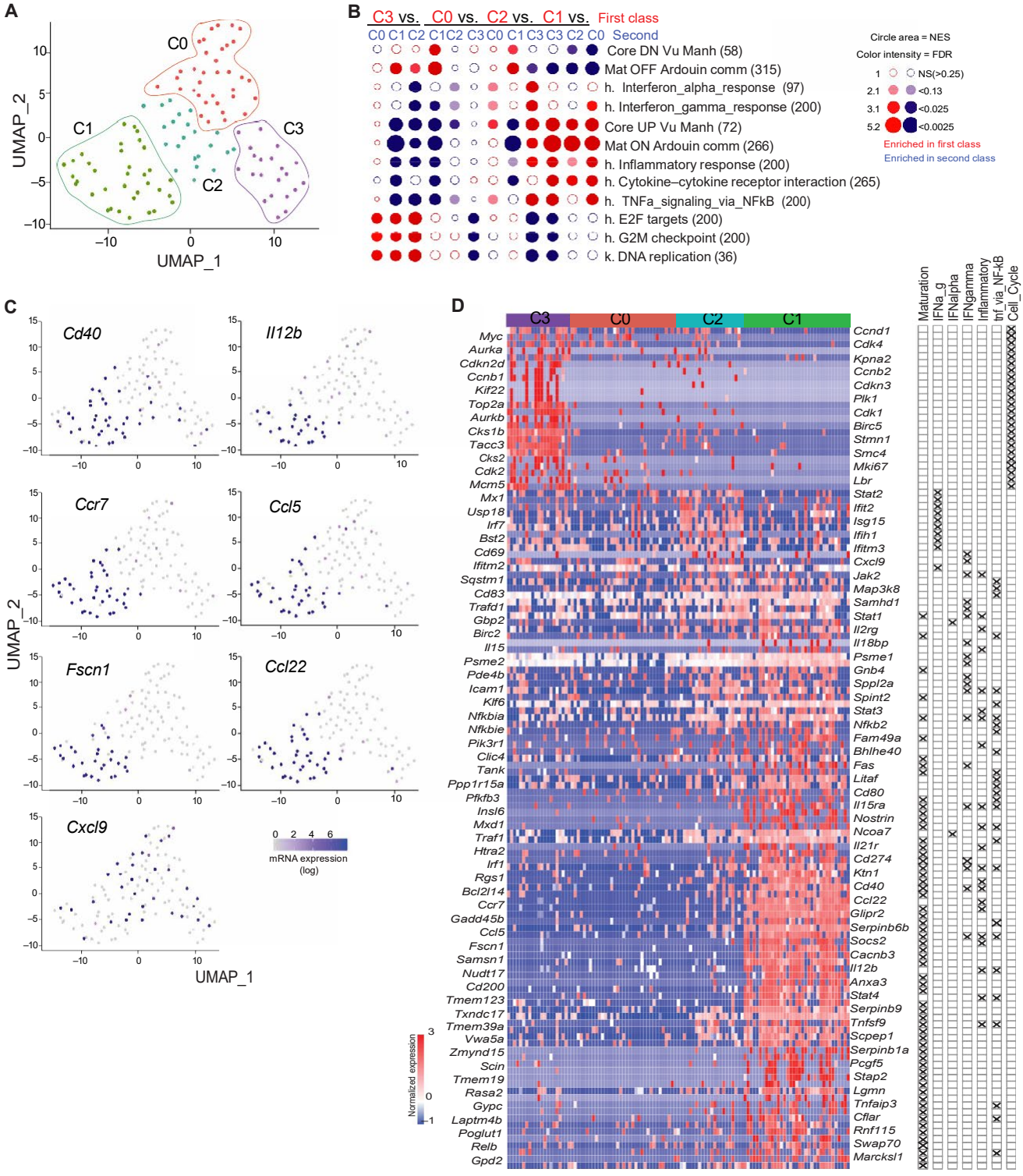


Fig. 2. Single-cell transcriptional profiling of cDC1s from immunogenic tumors. (**A**) Dimensionality reduction performed using the UMAP algorithm and graph-based cell clustering using Seurat, for 113 bona fide cDC1s sorted from YUMM1.7 tumors of eight female mice 10 days after engraftment. (**B**) BubbleMap showing results of GSEA with hallmark (h), KEGG pathway (k), and published DC maturation gene sets, performed by using BubbleGUM on pairwise comparisons between the clusters C0 to C3 shown in (A). Circle area indicates NES and color intensity the FDR. FDR was further corrected for multiple testing, leading to a higher stringency of the significance threshold. Core_DN_Vu_Manh and Core_UP_Vu_Manh correspond to gene sets down- or up-regulated, respectively, across human and mouse DC subsets during maturation in response to microbial stimuli (*29*). Mat_ON_Ardouin_comm and Mat_OFF_Ardouin_comm correspond to gene sets up- or down-regulated, respectively, during steady-state maturation of mouse cDC1s (*31*). Numbers in parentheses correspond to the number of genes. NS, not significant. (**C**) Expression levels of selected genes related to DC maturation, projected onto the UMAP space. (**D**) Heatmap showing expression of selected genes across C0 to C3 and association of individual genes to gene sets used in (B) (right).

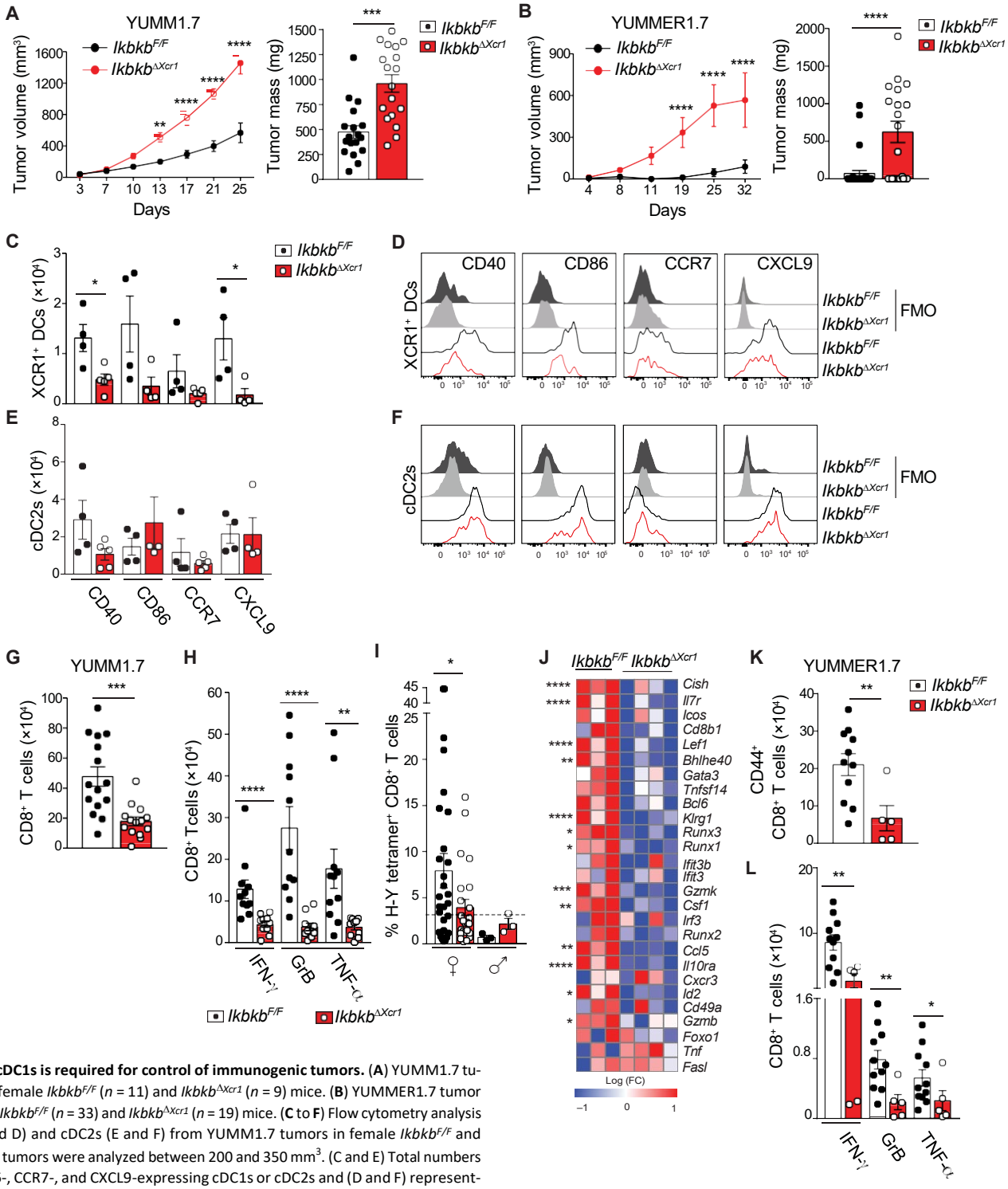


Fig. 3. IKKβ in cDC1s is required for control of immunogenic tumors. (**A**) YUMM1.7 tumor growth in female *Ikbkb*$^{F/F}$ (n = 11) and *Ikbkb*$^{\Delta Xcr1}$ (n = 9) mice. (**B**) YUMMER1.7 tumor growth in male *Ikbkb*$^{F/F}$ (n = 33) and *Ikbkb*$^{\Delta Xcr1}$ (n = 19) mice. (**C** to **F**) Flow cytometry analysis of cDC1s (C and D) and cDC2s (E and F) from YUMM1.7 tumors in female *Ikbkb*$^{F/F}$ and *Ikbkb*$^{\Delta Xcr1}$ mice; tumors were analyzed between 200 and 350 mm^3. (C and E) Total numbers of CD40-, CD86-, CCR7-, and CXCL9-expressing cDC1s or cDC2s and (D and F) representative histograms of flow cytometry analysis including fluorescence minus one (FMO) control. (**G**) Total number of CD8$^+$ T cells and (**H**) numbers of IFN-γ–, GrB-, or TNF-α–expressing CD8$^+$ T cells in YUMM1.7 tumors from female *Ikbkb*$^{F/F}$ and *Ikbkb*$^{\Delta Xcr1}$ mice; tumors were analyzed between 250 and 400 mm^3. (**I**) Frequency of H-Y–specific tumor-infiltrating CD8$^+$ T cells in YUMM1.7 tumors from female and male *Ikbkb*$^{F/F}$ and *Ikbkb*$^{\Delta Xcr1}$ mice. (**J**) High-throughput gene expression analysis (BioMark HD, Fluidigm) of tumor-infiltrating CD8$^+$ T cells from YUMM1.7 tumors in female *Ikbkb*$^{F/F}$ and *Ikbkb*$^{\Delta Xcr1}$ mice; statistical significance is indicated. FC, fold change. (**K**) Total numbers of CD44$^+$ CD8$^+$ T cells and (**L**) IFN-γ–, GrB-, and TNF-α–expressing CD44$^+$ CD8$^+$ T cells in TDLN from male *Ikbkb*$^{F/F}$ and *Ikbkb*$^{\Delta Xcr1}$ mice bearing YUMMER1.7 tumors; tumors were analyzed between 250 and 400 mm^3. Total cell numbers are indicated for 250 mg of tumor tissue. Pooled or representative data are shown from at least two independent experiments. Data are shown as means ± SEM. In scatter plots, each point corresponds to an individual mouse. Statistical analysis was performed by two-way ANOVA followed by Sidak's multiple comparison tests [(A and B), tumor volume graphs], Mann-Whitney test, or multiple unpaired t test (J). Fisher's exact test was used for frequency of tetramer$^+$ cells when their proportion was above the highest level obtained with HPV16 E7$_{(49–57)}$/H-2D^b tetramer (I).

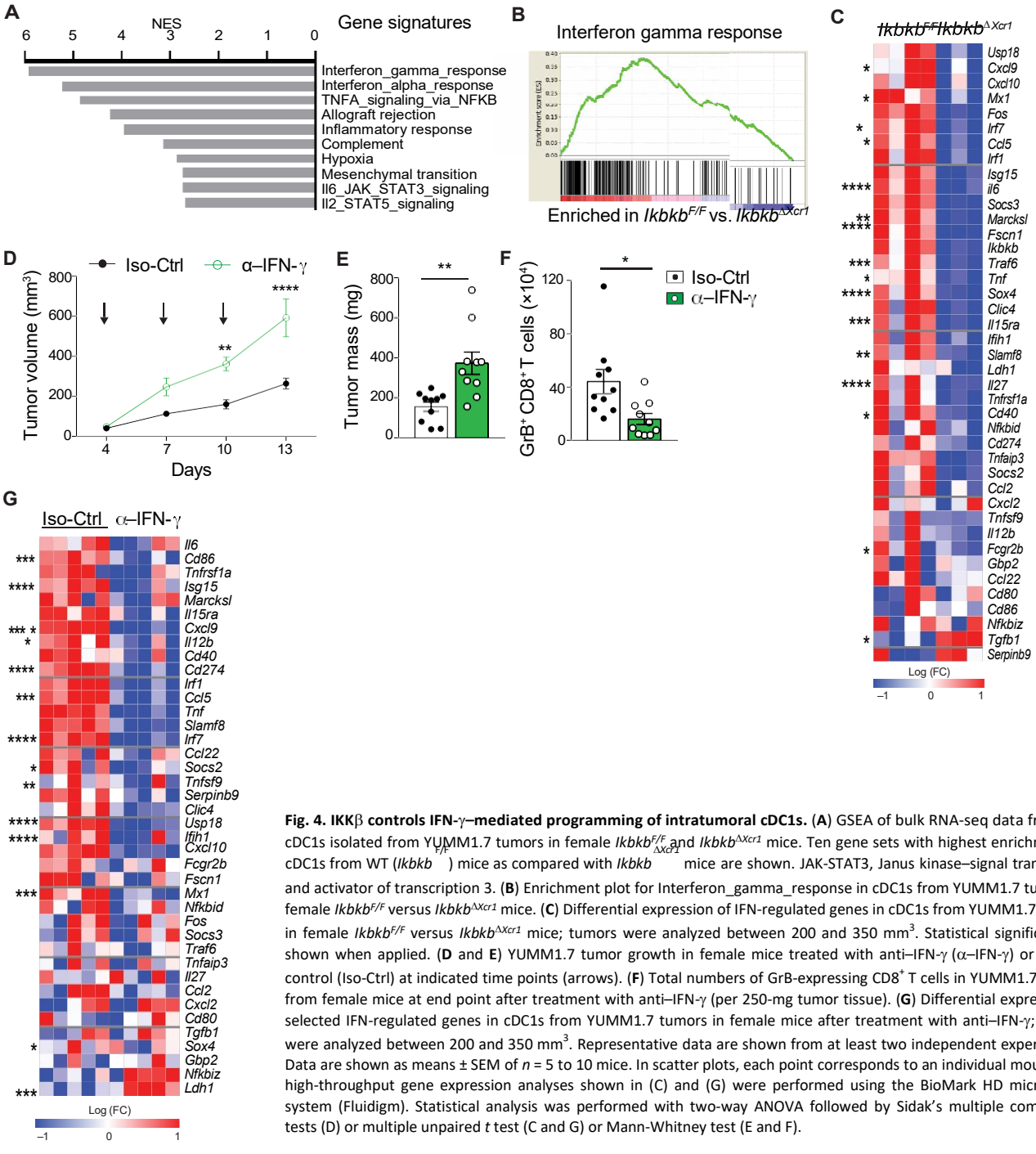


Fig. 4. IKKβ controls IFN-γ–mediated programming of intratumoral cDC1s. (**A**) GSEA of bulk RNA-seq data from cDC1s isolated from YUMM1.7 tumors in female *Ikbkb*$^{F/F}$ and *Ikbkb*$^{\Delta Xcr1}$ mice. Ten gene sets with highest enrichment in cDC1s from WT (*Ikbkb*$^{F/F}$) mice as compared with *Ikbkb*$^{\Delta Xcr1}$ mice are shown. JAK-STAT3, Janus kinase–signal transducer and activator of transcription 3. (**B**) Enrichment plot for Interferon_gamma_response in cDC1s from YUMM1.7 tumors in female *Ikbkb*$^{F/F}$ versus *Ikbkb*$^{\Delta Xcr1}$ mice. (**C**) Differential expression of IFN-regulated genes in cDC1s from YUMM1.7 tumors in female *Ikbkb*$^{F/F}$ versus *Ikbkb*$^{\Delta Xcr1}$ mice; tumors were analyzed between 200 and 350 mm^3. Statistical significance is shown when applied. (**D** and **E**) YUMM1.7 tumor growth in female mice treated with anti–IFN-γ (α–IFN-γ) or isotype control (Iso-Ctrl) at indicated time points (arrows). (**F**) Total numbers of GrB-expressing CD8$^+$ T cells in YUMM1.7 tumors from female mice at end point after treatment with anti–IFN-γ (per 250-mg tumor tissue). (**G**) Differential expression of selected IFN-regulated genes in cDC1s from YUMM1.7 tumors in female mice after treatment with anti–IFN-γ; tumors were analyzed between 200 and 350 mm^3. Representative data are shown from at least two independent experiments. Data are shown as means ± SEM of $n = 5$ to 10 mice. In scatter plots, each point corresponds to an individual mouse. The high-throughput gene expression analyses shown in (C) and (G) were performed using the BioMark HD microfluidic system (Fluidigm). Statistical analysis was performed with two-way ANOVA followed by Sidak's multiple comparison tests (D) or multiple unpaired *t* test (C and G) or Mann-Whitney test (E and F).

most of these genes, confirming the NF-κB–dependent control of the IFN-γ response in intratumoral cDC1s (Fig. 4C). This prompted us to assess the impact of IFN-γ signaling on cDC1 functionality during immunogenic tumor growth. For this purpose, we treated female YUMM1.7 tumor–bearing mice with IFN-γ–neutralizing antibody. This resulted in a significant increase in tumor growth (Fig. 4, D and E) and reduction in tumor-infiltrating effector CD8$^+$ T cells (Fig. 4F). We then measured the expression of hallmark IFN-γ–induced genes in cDC1s isolated from these tumors. In line with the conditional deletion of IKKβ in cDC1s, IFN-γ neutralization reduced the expression of most of these genes (Fig. 4G), which confirmed the association between NF-κB activation and induction of IFN-γ–responsive genes in intratumoral cDC1s.

NF-κB/IFN-γ–dependent genes in tumor-associated cDC1s included both *Cxcl9* and *Cxcl10* (Fig. 4, C and G), which are major chemoattractants for CXCR3-expressing effector CD8$^+$ T cells (*1*, *33*, *34*). CXCL9 production by DCs has been suggested to play a key role in the recruitment of effector CD8$^+$ T cells to tumors (*1*).

We observed a significant reduction in CXCL9-expressing cDC1s in *Ikbkb*$^{\Delta Xcr1}$ mice compared with littermate controls (Fig. 3, C and D, and fig. S4G). In addition, uncontrolled tumor growth in *Ikbkb*$^{\Delta Xcr1}$ mice correlated with reduced accumulation of activated CD8$^+$ T cells (Fig. 3, G to L). To evaluate the contribution of CXCR3 ligands to the control of tumor growth, we treated female YUMM1.7 tumor–bearing mice with CXCR3-blocking antibody. As observed with IKKβ deletion in cDC1s and with IFN-γ neutralization, CXCR3 blockade impaired the recruitment of tumor-infiltrating CD8$^+$ T cells and increased tumor growth (fig. S5, A to C). To evaluate the specific contribution of cDC1-derived CXCL9, we generated mice with a conditional deletion of *Cxcl9* in cDC1s (*Cxcl9*$^{\Delta Xcr1}$) (fig. S5, D and E). YUMM1.7 tumor growth and T cell recruitment was not altered in *Cxcl9*$^{\Delta Xcr1}$ mice (fig. S5, F to H), suggesting that CXCL9 expression by cDC1s was not required for CD8$^+$ T cell recruitment and control of tumor growth in this model. Similar results were also observed in mice bearing a germline deletion in Cxcl9 (*Cxcl9*$^{\Delta/\Delta}$) (fig. S5, I to M). Given that CXCR3 blockade impaired T cell recruitment and significantly increased tumor growth in this model, these data suggest redundancy between CXCL9 and other CXCR3 ligands such as CXCL10. These results also highlight the importance of NF-κB activation in cDC1s for driving their expression of multiple genes that contribute to CD8$^+$ T cell recruitment and antitumoral functions, including *Cxcl10*, *Ccl5*, and *Il12b*, besides *Cxcl9*.

NF-κB–mediated IFN regulatory factor 1 expression in cDC1s is required for control of immunogenic tumors

Among the NF-κB– and IFN-γ–regulated genes in tumor-associated cDC1s was the transcription factor IRF1 (IFN regulatory factor 1) (Fig. 4, C and G), which is a master regulator of IFN-mediated gene expression (*35*) and also enriched during intratumoral cDC1 maturation (fig. S2C). We therefore sought to determine the role of IRF1 in the NF-κB–dependent control of cDC1-mediated antitumor immunity. To this end, we generated mice with a conditional deletion of IRF1 in cDC1s (*Irf1*$^{\Delta Xcr1}$). We confirmed efficient deletion of IRF1 specifically in cDC1s from *Irf1*$^{\Delta Xcr1}$ mice at mRNA and protein levels (fig. S6, A to D). Unlike *Ikbkb*$^{\Delta Xcr1}$ mice, IRF1 deletion did not affect accumulation of migratory cDC1s in steady state (fig. S6, E and F), indicating that IRF1 did not regulate steady-state cDC1 maturation. In addition, we did not observe an increase in CD11c^{hi} cDC2s in *Irf1*$^{\Delta Xcr1}$ mice (fig. S6G), contrary to what was seen in *Xcr1*^{DTA} mice (fig. S1, E and F).

We then transplanted cohorts of male or female *Irf1*$^{\Delta Xcr1}$ mice and littermate controls with YUMM1.7 tumors, or only male mice with YUMMER1.7 tumors. As we had observed in *Xcr1*^{DTA} and *Ikbkb*$^{\Delta Xcr1}$ mice, growth of YUMM1.7 tumors was unaffected in male *Irf1*$^{\Delta Xcr1}$ mice (fig. S6H), but tumor growth was significantly increased in female *Irf1*$^{\Delta Xcr1}$ mice compared with controls (Fig. 5A). Similarly, about half of male *Irf1*$^{\Delta Xcr1}$ mice failed to control growth of YUMMER1.7 tumors (Fig. 5B). In line with data from *Ikbkb*$^{\Delta Xcr1}$ mice, the accumulation of cDC1s in YUMM1.7 tumors from female *Irf1*$^{\Delta Xcr1}$ mice was unaffected (fig. S6I), but their expression of maturation markers CD40 and CD86 and CXCL9 was significantly impaired (Fig. 5C). In contrast, tumor-associated cDC2s in *Irf1*$^{\Delta Xcr1}$ mice were unaffected (fig. S6J). Furthermore, the expression of NF-κB–dependent IFN-γ–responsive genes, including *Cxcl10*, *Ccl5*, *Il12b*, and *Cxcl9*, was down-regulated in intratumoral cDC1s from *Irf1*$^{\Delta Xcr1}$ mice (Fig. 5D). Consistent with the increased growth of YUMM1.7 tumors in female *Irf1*$^{\Delta Xcr1}$ mice, the frequency of tumor-infiltrating H-Y–specific CD8$^+$ T cells was significantly reduced (Fig. 5E and fig. S6K), as was the global recruitment and activation of tumor-infiltrating effector CD8$^+$ T cells (Fig. 5, F to H). Similarly, the frequency of activated CD8$^+$ T cells in TDLNs after engraftment with YUMMER1.7 tumors was significantly reduced in *Irf1*$^{\Delta Xcr1}$ mice (Fig. 5, I and J).

These data demonstrated that IRF1, along with NF-κB, was required for the cDC1-mediated control of immunogenic tumors. Furthermore, IRF1 was necessary for the induction of a subset of NF-κB–dependent and IFN-γ–responsive genes in intratumoral cDC1s, including *Cxcl9*, *Cxcl10*, *Ccl5*, *Cd40*, and *Il12b* (fig. S6L), suggesting a hierarchical relationship in which NF-κB upstream of IRF1 activation in cDC1s is required for control of immunogenic tumor growth.

NF-κB and IRF1 coordinate maturation of tumor-infiltrating cDC1s

To further dissect the impact of NF-κB and IRF1–regulated pathways on the intratumoral maturation of cDC1s, we performed scRNA-seq analysis on cDC1s from YUMM1.7 tumor–bearing mice after targeted deletion of IKKβ or IRF1. We analyzed a total of 361 index-sorted bona fide cDC1s, using FB5P-seq, and performed unsupervised Seurat clustering analysis. We identified seven distinct cDC1 clusters based on their gene expression (Fig. 6A). The frequency of the different clusters in WT (*Ikbkb*$^{F/F}$/*Irf1*$^{F/F}$) and *Ikbkb*$^{\Delta Xcr1}$ or *Irf1*$^{\Delta Xcr1}$ mice was largely similar, except for an increase of C4 in both *Ikbkb*- and *Irf1*-deficient cDC1s (Fig. 6B). GSEA revealed enrichment of cell proliferation GSs in C5 and, to a lesser extent, C6 (Fig. 6C), which was similar to C3 in the previous analysis of WT cDC1s (WT-C3) (Fig. 2B and fig. S7A). C1 and C2 were enriched for inflammatory pathways and DC maturation genes (Fig. 6, C, D, and G, and fig. S7B), representing the counterparts of the mature cDC1s identified among WT cDC1s (WT-C1) (fig. S7A). In contrast, C3 was enriched for immature DC gene sets and expressed the lowest levels of DC maturation genes (Fig. 6, C and D), mirroring the cluster of immature WT cDC1s identified previously (WT-C0 in Fig. 2A).

To evaluate the possible dynamics between these different clusters, we performed single-cell trajectory inference using Monocle (*36*). This unsupervised learning algorithm inferred a branched trajectory of cDC1s with three end points at C5, C3, and C2 (Fig. 6E). Because C2 expressed the highest enrichment for DC maturation genes (Fig. 6C), which were negatively enriched in C3 and C5, we considered C3 and C5 as alternative roots for a cDC1 maturation end point at C2 (Fig. 6E). These two alternative paths for cDC1 maturation converged at C4, before reaching the fully mature state represented by C2 (Fig. 6, E and F). This analysis pinpointed C4 as a possible transitory state for intratumoral cDC1 maturation. C4 showed a particular enrichment for IFN-responsive genes, as well as an induction of DC maturation gene sets (Fig. 6C). The proportion of cells in C4 substantially increased upon deletion of NF-κB or IRF1 (Fig. 6B), pointing to a possible role for NF-κB/IRF1 signaling in promoting the exit of cDC1s from this IFN-responsive state (C4) into their fully mature state (C2). In keeping with this hypothesis, both NF-κB signaling and IRF1 expression were mostly enriched in fully mature cDC1s (C1 and C2) (Fig. 6C and fig. S7C). Furthermore, the genes up-regulated in C1 and C2 compared with C4, including *Ccl5*, *Il12b*, *Cd40*, and *Fscn1* (fig. S7, B and D), were down-regulated in both NF-κB and IRF1 deficient intratumoral cDC1s (Figs. 4C and 5D and fig. S7, D to F). The transcripts down-regulated in intratumoral cDC1s upon IKKβ and IRF1 deletion also included genes associated with antigen processing and presentation (e.g.,

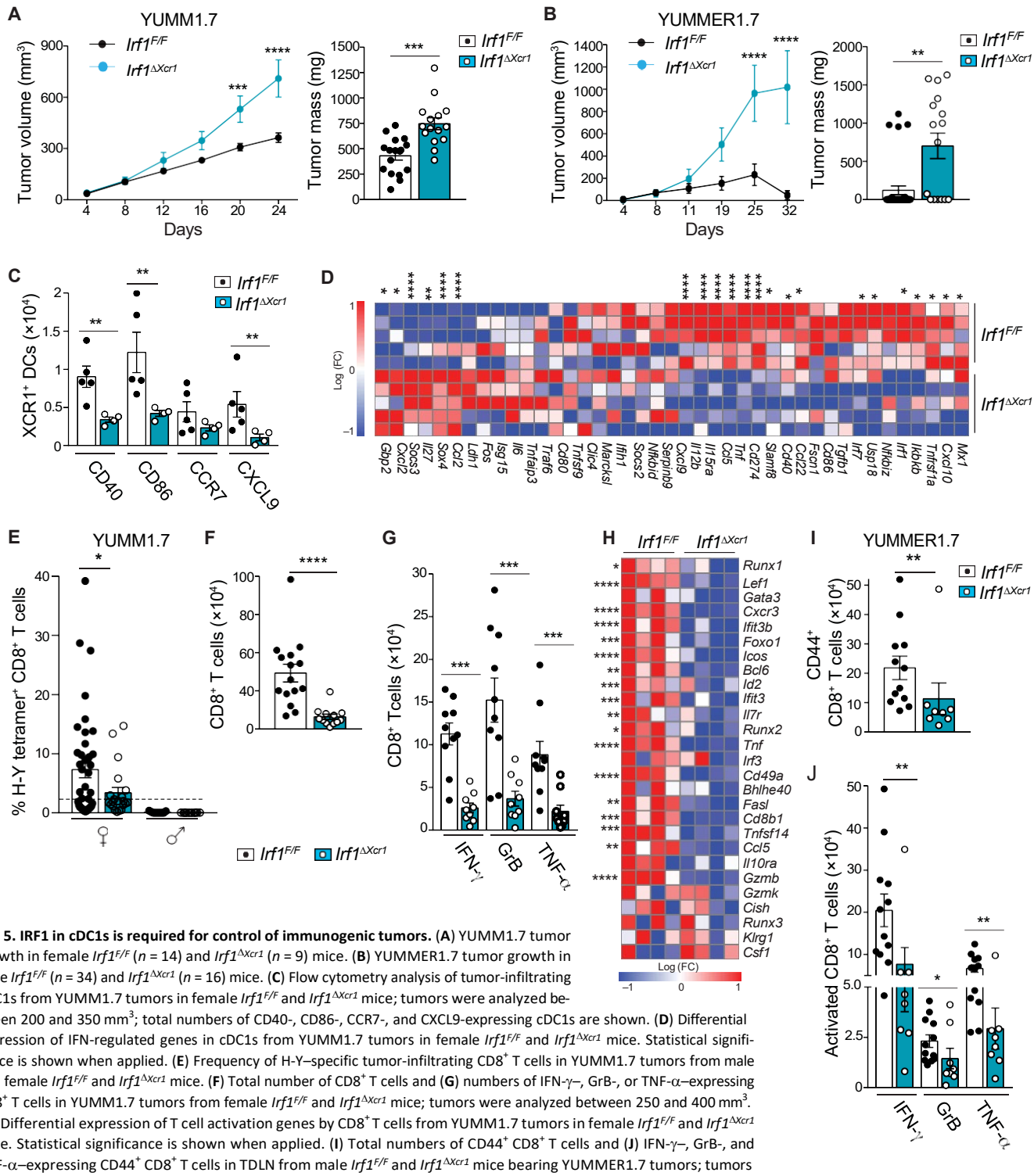


Fig. 5. IRF1 in cDC1s is required for control of immunogenic tumors. (**A**) YUMM1.7 tumor growth in female *Irf1*$^{F/F}$ (n = 14) and *Irf1*$^{\Delta Xcr1}$ (n = 9) mice. (**B**) YUMMER1.7 tumor growth in male *Irf1*$^{F/F}$ (n = 34) and *Irf1*$^{\Delta Xcr1}$ (n = 16) mice. (**C**) Flow cytometry analysis of tumor-infiltrating cDC1s from YUMM1.7 tumors in female *Irf1*$^{F/F}$ and *Irf1*$^{\Delta Xcr1}$ mice; tumors were analyzed between 200 and 350 mm^3; total numbers of CD40-, CD86-, CCR7-, and CXCL9-expressing cDC1s are shown. (**D**) Differential expression of IFN-regulated genes in cDC1s from YUMM1.7 tumors in female *Irf1*$^{F/F}$ and *Irf1*$^{\Delta Xcr1}$ mice. Statistical significance is shown when applied. (**E**) Frequency of H-Y–specific tumor-infiltrating CD8$^+$ T cells in YUMM1.7 tumors from male and female *Irf1*$^{F/F}$ and *Irf1*$^{\Delta Xcr1}$ mice. (**F**) Total number of CD8$^+$ T cells and (**G**) numbers of IFN-γ–, GrB-, or TNF-α–expressing CD8$^+$ T cells in YUMM1.7 tumors from female *Irf1*$^{F/F}$ and *Irf1*$^{\Delta Xcr1}$ mice; tumors were analyzed between 250 and 400 mm^3. (H) Differential expression of T cell activation genes by CD8$^+$ T cells from YUMM1.7 tumors in female *Irf1*$^{F/F}$ and *Irf1*$^{\Delta Xcr1}$ mice. Statistical significance is shown when applied. (**I**) Total numbers of CD44$^+$ CD8$^+$ T cells and (**J**) IFN-γ–, GrB-, and TNF-α–expressing CD44$^+$ CD8$^+$ T cells in TDLN from male *Irf1*$^{F/F}$ and *Irf1*$^{\Delta Xcr1}$ mice bearing YUMMER1.7 tumors; tumors were analyzed between 250 and 400 mm^3. Total cell numbers are indicated for 250 mg of tumor tissue. Pooled or representative data are shown from at least two independent experiments. Data are shown as means ± SEM. In scatter plots, each point corresponds to an individual mouse. The high-throughput gene expression analyses shown in (D) and (H) were performed using the BioMark HD microfluidic system (Fluidigm). Statistical analysis was performed by two-way ANOVA followed by Sidak's multiple comparison tests [(A and B), tumor volume graphs], Mann-Whitney test, or multiple unpaired t test (D and H). Fisher's exact test was used for frequency of tetramer$^+$ cells when their proportion above the highest level obtained with HPV16 E7$_{(49–57)}$/H-2D^b tetramer (E).

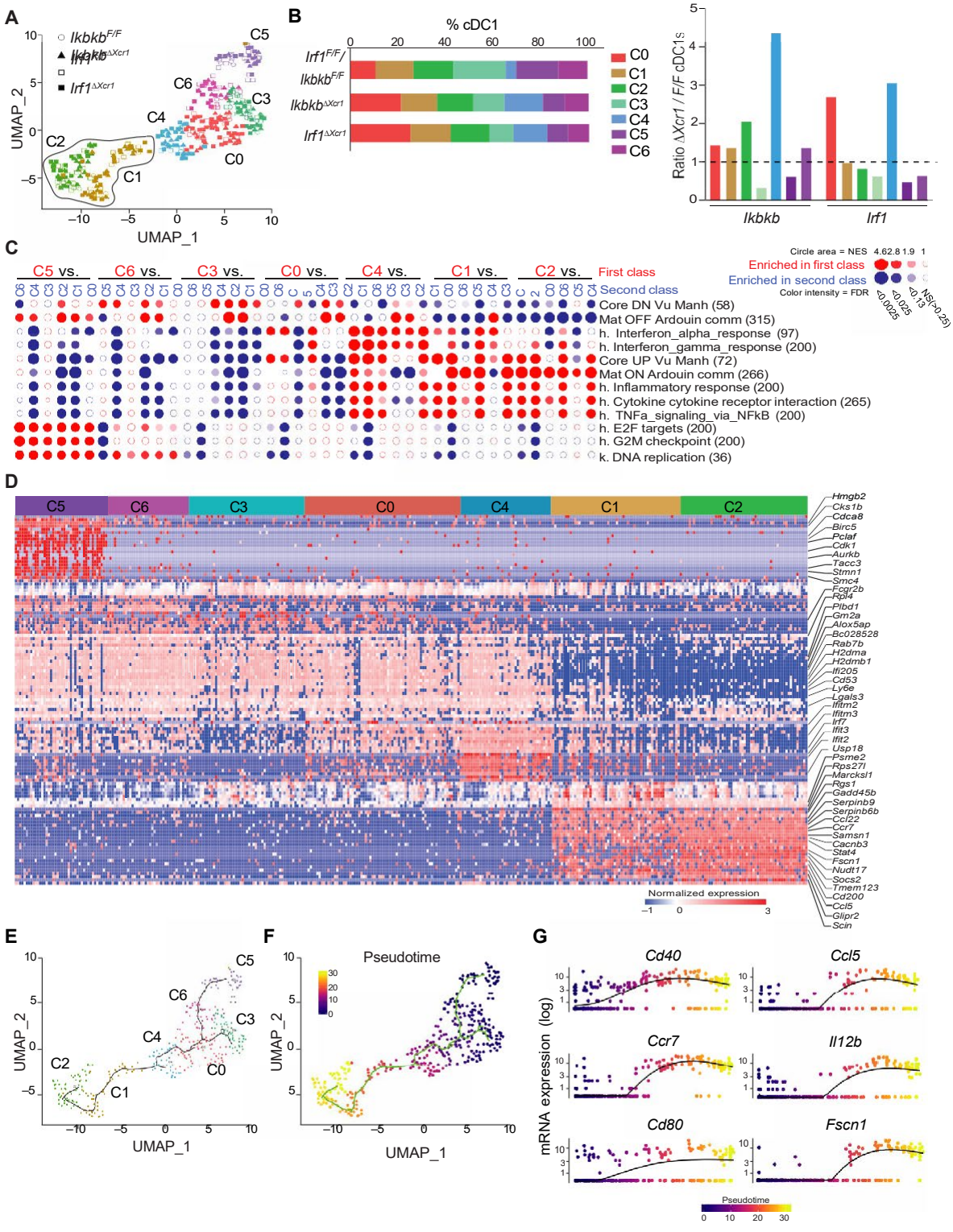


Fig. 6. IKKβ and IRF1 coordinate intratumoral cDC1 maturation. (**A**) UMAP and graph-based cell clustering for 360 bona fide cDC1s isolated from YUMM1.7 tumors of 16 female *Ikbkb*$^{F/F}$, *Ikbkb*$^{\Delta XCR1}$, *Irf1*$^{F/F}$, and *Irf1*$^{\Delta Xcr1}$ mice grown to a volume of 200 to 350 mm^3; seven distinct clusters are indicated C0 to C6. (**B**) Distribution of clusters among total cDC1s in each group (left) and proportions of individual cDC1 clusters in *Ikbkb*$^{\Delta Xcr1}$ and *Irf1*$^{\Delta Xcr1}$ mice relative to their respective littermate controls (*Ikbkb*$^{F/F}$ and *Irf1*$^{F/F}$) (right). (**C**) BubbleMap showing the results of GSEA using hallmark, KEGG pathway, and published DC maturation gene sets performed with BubbleGUM for pairwise comparisons between clusters C0 to C6 shown in (A), as described in Fig. 2B. (**D**) Heatmap showing expression levels of selected genes across C0 to C6. (**E** and **F**) Single-cell trajectory inference by Monocle with projection onto the UMAP space, (E) showing Seurat clusters and (F) the pseudotime analysis using C5 as the root. (**G**) Expression pattern along Monocle pseudotime of selected genes related to cDC1.

Tapbp and *Psmb1*), as well as DC maturation and IFN response pathways (fig. S7, D to F). Therefore, *Ikbkb* and *Irf1* deletion in cDC1s qualitatively altered the functional maturation of intratumoral cDC1s, although the trajectory of cDC1 maturation was largely unaffected. These data support a role for NF-κB/IRF1 signaling in promoting the functional maturation of intratumoral cDC1s, including antigen presentation as well as cytokine and chemokine production, leading to recruitment and activation of effector T cells.

To explore the transcriptional regulation of distinct cDC1 clusters, we used Distant Regulatory Elements of Co-regulated Genes (DiRE) analysis to look for enrichment of specific regulatory elements from the TRANSFAC database among the differentially expressed genes (DEGs) from each cluster (fig. S7H). We also performed transcription factor binding site analysis using the Encyclopedia of DNA Elements (ENCODE) chromatin immunoprecipitation-sequencing (ChIP-seq) database (fig. S7I). In agreement with the results of GSEA, this analysis showed a selective enrichment of NF-κB target genes in mature cDC1s (C1 and C2) and IRF/signal transducer and activator of transcription target genes in C4—known regulators of IFN response pathways. Moreover, consistent with IRF1 acting down-stream of NF-κB activation, an EnrichR analysis of DEGs down-regulated upon IKKβ deletion in cDC1s using transcription factor PPI database revealed a network including three members of the IRF family that emerged with high combined scores, of which IRF1 had the highest number of interactions within the network (fig. S7, J and K). On the other hand, analysis of DEGs down-regulated in $Irf1^{\Delta Xcr1}$ cDC1s did not show enrichment for NF-κB signaling (fig. S7, L and M), suggesting that NF-κB was not directly implicated downstream of IRF1 signaling in cDC1s. In addition, *Irf1* expression was reduced in mature cDC1s (C2) from $Ikbkb^{\Delta Xcr1}$, whereas *Ikbkb* expression was not affected in cDC1s from $Irf1^{\Delta Xcr1}$ mice (fig. S7N). Together, these data suggest that an NF-κB/IRF1 axis coordinates the maturation of tumor-infiltrating cDC1s, and we have pinpointed a transitional activation state that is highly dependent on NF-κB and IRF1 signaling for progression to a fully mature functional state.

To extend our observations to other tumor models, we analyzed the expression of NF-κB/IRF1 codependent genes in scRNA-seq data from cDC1s in a previous study from a mouse model of lung adenocarcinoma (LUAD) (*15*). We first reconstructed Seurat clustering of cDC1s from naïve and tumor-bearing lungs in this dataset [Gene Expression Omnibus (GEO) accession no. GSE131957). This identified eight distinct clusters visualized by UMAP (C0 to C7) (fig. S8A). We next performed a Jaccard similarity analysis to compare these clusters with the cDC1 clusters that we identified in YUMM1.7 melanomas (YUMM-C0/C6). The highest Jaccard index (JI) was obtained between C7 of lung tumor–associated cDC1s and YUMM-C1/C2 mature cDC1s (fig. S8B), suggesting a similar maturation state between tumor-associated cDC1s in murine melanomas and LUADs. Among lung cDC1s, IKKβ and IRF1 were also most highly expressed by cells with a mature phenotype (C7), as compared with any other cluster (fig. S8D). This was accompanied by the highest expression levels of NF-κB/IRF1–dependent genes involved in IFN-γ response (fig. S8D) and DC maturation (fig. S8C). Mature cDC1s in normal mouse lung tissue did not show a concerted up-regulation of IKKβ and IRF1 (fig. S8E), suggesting that NF-κB and IRF1 activation in cDC1s is up-regulated in response to specific signals in the tumor microenvironment.

In summary, we have described in a clinically relevant mouse model of melanoma the coordinated regulation of intratumoral cDC1 maturation by NF-κB upstream of IRF1, which are both required to control immunogenic tumor growth. In addition, the implication of the NF-κB/IRF1 axis in intratumoral cDC1 maturation appears to be conserved in other cancer models.

The NF-κB/IRF1 axis in cDC1s correlates with good prognosis in patients with melanoma

We next sought to determine the relevance of NF-κB and IRF1 signaling in cDC1s to human cancer. We first deconvoluted the gene expression data from The Cancer Genome Atlas (TCGA) for skin cutaneous melanoma (SKCM; 468 patients). We used a previously published gene list for cDC1s from this dataset (*37*) and scored the expression of these genes in addition to *IRF1* and two hallmark transcripts of the NF-κB pathway (*IKBKB* and *NFKB1*) (Fig. 7A). Hierarchical clustering showed consistency between *IRF1*, *IKBKB*, and *NFKB1* and the human cDC1 GS; therefore, we included these genes in the cDC1 signature for inference of NF-κB/IRF1 pathway enrichment in cDC1s. Individually, IRF1 showed a stronger correlation than NFKB1/IKBKB with the cDC1 signature (fig. S9). This is likely due to the broader roles of NFKB in tumors, which are well documented. This also suggests a more specific impact of IRF1 and cDC1s in tumors, which is in keeping with our data in mouse models (fig. S6). To derive the most appropriate transcripts for the identification of activated $CD8^+$ T cells, we selected the most relevant genes specific to $CD8^+$ T cells that were altered upon IKKβ or IRF1 deletion in cDC1s in our mouse melanoma model (Fig. 7B). In line with the established role of cDC1s in recruitment of tumor-infiltrating $CD8^+$ T cells, the cDC1 signature showed a high degree of positive correlation with the activated $CD8^+$ T cell signature (Fig. 7C). To discern whether this observation was relevant for disease prognosis, we analyzed the survival of patients with melanoma with high (top quartile) and low (bottom quartile) levels of cDC1 alone and NF-κB/IRF1–enriched cDC1 signatures. We found that the NF-κB/IRF1–enriched cDC1 signature was associated with improved prognostic outcome in patients with melanoma compared with the cDC1 signature alone (Fig. 7D).

To further explore the implication of the NF-κB/IRF1 axis in cDC1s for human melanoma, we analyzed the expression of NF-κB/IRF1 co-regulated cytokine genes that we had identified in cDC1s from our mouse melanoma model, and which were also linked to $CD8^+$ T cell recruitment and activation (*CCL5*, *CCL22*, *CXCL9*, *CXCL10*, and *IL12B*) (Fig. 7E). These cytokines are highly expressed in activated DCs compared with other immune cells in human cancers. This NF-κB/IRF1–dependent cytokine signature was highly correlated with the activated $CD8^+$ T cell signature and showed a higher correlation with the NF-κB/IRF1–enriched cDC1 signature than with the cDC1 signature alone (Fig. 7F), supporting a role for the NF-κB/IRF1 axis in expression of these cytokines and recruitment of cytotoxic $CD8^+$ T cells in patients with melanoma. Consistent with this observation, high expression of both the activated $CD8^+$ T cell signature and the NF-κB/IRF1–dependent cytokine signature was significantly associated with patient survival (Fig. 7G). To account for cDC1-independent NF-κB/IRF1 expression in our analysis, which is more likely in patients with melanoma bearing a low cDC1 score, we focused our analysis on data from patients bearing high cDC1 GSs. In this analysis, we compared the score of activated $CD8^+$ T cells and NF-κB/IRF1–dependent cytokines between individuals with high (top quartile) and low (bottom quartile) levels of *IRF1* and *IKBKB/NFKB1* gene expression. This revealed that among

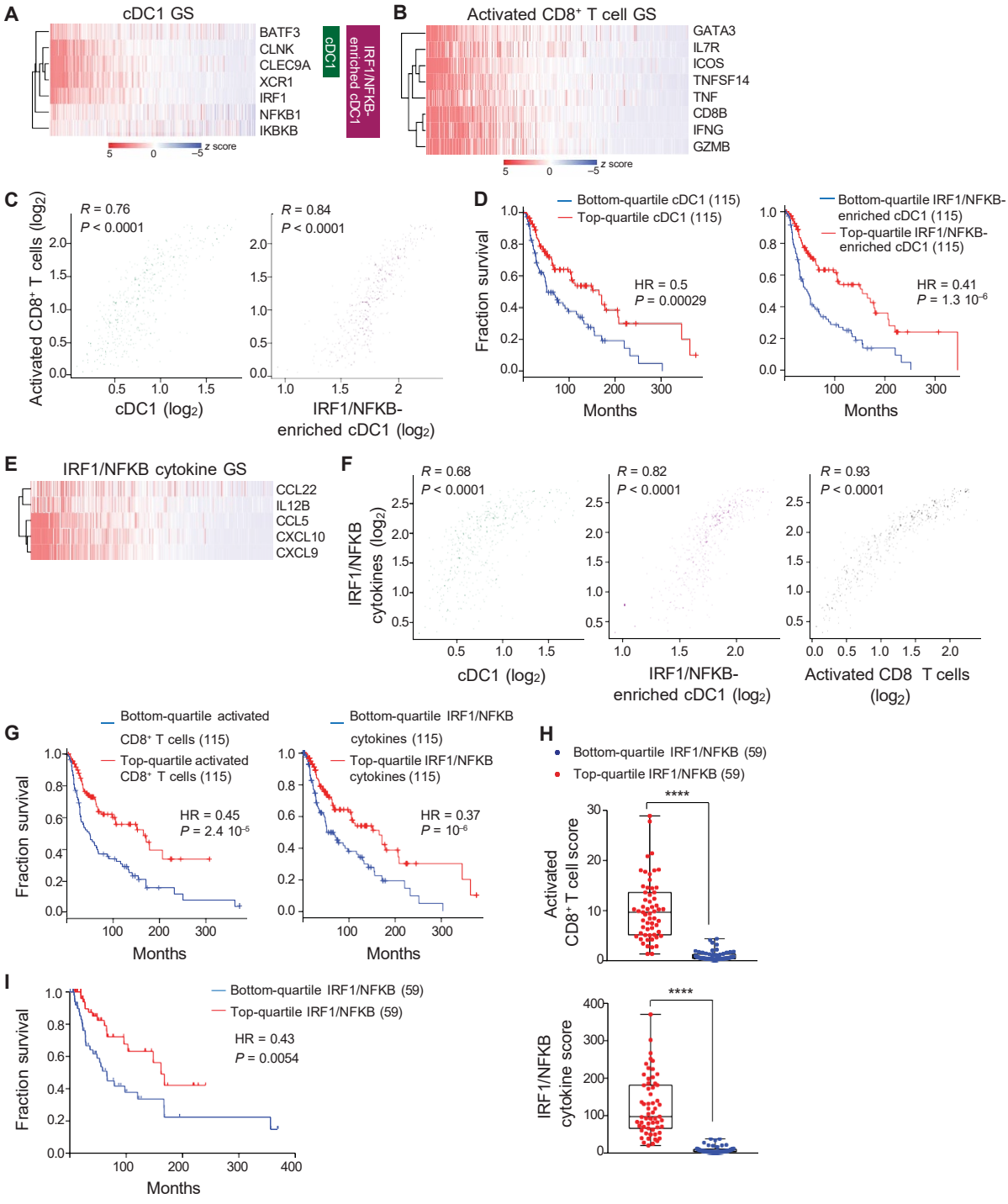


Fig. 7. NF-κB/IRF1–enriched cDC1 GSs correlate with increased survival in patients with melanoma. (**A**) Heatmap showing the gene similarity–ordered, *z*-transformed expression values for cDC1 and NFKB/IRF1-enriched cDC1 GSs and (**B**) activated CD8$^+$ T cell GS in patients with melanoma from TCGA datasets. CLNK, cytokine-dependent hematopoietic cell linker. CLEC9A (C-type lectin domain containing 9A), CLNK (cytokine dependent hematopoietic cell linker). (**C**) Spearman correlation between cDC1 GS or NFKB/IRF1-enriched cDC1 GS with activated CD8$^+$ T cell GS in melanoma TCGA datasets. (**D**) Kaplan-Meier overall survival curves of TCGA patients with melanoma comparing top and bottom quartiles of cDC1 GS or NFKB/IRF1-enriched cDC1 GS. Hazard ratio (HR) and *P* value from univariate Cox regression are indicated. (**E**) Heatmap showing the gene similarity–ordered, *z*-transformed expression values for NFKB/IRF1-dependent chemokine GS in melanoma TCGA datasets. (**F**) Spearman correlation between cDC1 GS, NFKB/IRF1-enriched cDC1 GS, and activated CD8$^+$ T cell GS with NFKB/IRF1-dependent chemokine GS in melanoma TCGA datasets. (**G**) Kaplan-Meier overall survival curves of TCGA patients with melanoma comparing top and bottom quartiles of activated CD8$^+$ T cell GS or NFKB/IRF1-dependent chemokine GS. (**H**) Box plots comparing activated CD8$^+$ T cell GS and NFKB/IRF1-dependent chemokine GS in top and bottom quartiles of NFKB/IRF1 expression in TCGA patients with melanoma bearing high cDC1 GS (top 50%). (**I**) Kaplan-Meier overall survival curve comparing top and bottom quartiles of NFKB/IRF1 expression in TCGA patients with melanoma bearing high cDC1 GS score (top 50%).

patients bearing high cDC1 signatures, individuals with higher expression of *IKBKB*/*NFKB1* and *IRF1* showed a substantial increase in the CD8⁺ T cell signature and NF-κB/IRF1–dependent cytokine signature (Fig. 7H). Furthermore, *IKBKB*/*NFKB1* and *IRF1* expression correlated significantly with good prognosis for patients with melanoma bearing high cDC1 signatures (Fig. 7I). Although we cannot ascertain from this analysis that NF-κB/IRF1–dependent genes are exclusively or even dominantly expressed by intratumoral cDC1s, these findings point to a powerful influence of NF-κB and IRF1 in patients with melanoma and the interplay between tumor-associated cDC1s and CD8⁺ T cells that are critical factors in prognosis.

In addition, we performed similar analyses on LUAD from TCGA (fig. S10). The enrichment of IRF1/NFKB and the cDC1 signature increased the correlation with activated CD8⁺ T cells in LUAD (fig. S10, A, B, and D). The IRF1/NFKB-dependent cytokine signature also correlated highly with activated CD8⁺ T cells in this dataset (fig. S10, F and G). Unlike SKCM, the survival of patients with LUAD was only moderately associated with the activated CD8⁺ T cell and cDC1 signatures (fig. S10, E and H). However, the correlation between IRF1 or NFKB1/IKBKB expression and cDC1s was low in the LUAD dataset (fig. S10C), which may explain the lack of impact on survival of the IRF1/NFKB-enriched cDC1 signature in this dataset.

DISCUSSION

Several studies in preclinical mouse models and correlative analyses in patients with cancer support an important contribution of cDC1s to the efficacy of immunotherapy. However, the roles of cDC1s in relation to intrinsic tumor immunogenicity are less clear. Here, we examined the specific role of cDC1s in control of tumor growth in relation to tumor immunogenicity in a clinically relevant mouse melanoma model. We demonstrated that specific depletion of Xcr1-expressing cDC1s did not affect growth of nonimmunogenic tumors, where activated CD8⁺ T cells were scarce, but severely affected the control of immunogenic tumors, at least in part by preventing the recruitment of tumor-specific CD8⁺ T cells.

scRNA-seq revealed a cluster of cDC1s in tumors that was enriched for genes associated with DC maturation alongside NF-κB and IFN-regulated signaling pathways, indicating that these pathways may have an important role in intratumoral cDC1 maturation. We showed that targeted deletion of IKKβ impaired intratumoral cDC1 maturation and expression of IFN-γ–regulated genes, which was associated with increased tumor growth. These data suggest an intrinsic role of NF-κB signaling in the IFN-γ–mediated licensing of cDC1s and control of tumor growth. We identified IRF1, which is a known regulator of IFN response pathways, as an NF-κB–dependent gene in intratumoral cDC1s. Moreover, targeted deletion of IRF1 in Xcr1⁺ cDC1s phenocopied the deletion of IKKβ, providing genetic evidence for an NF-κB/IRF1 axis regulating the maturation of intratumoral cDC1s and control of immunogenic tumor growth. Several immune-suppressive genes were specifically up-regulated in IRF1-deficient cDC1s, including *Il27* (*38*), *Socs3* (*39*), *Fcgr2b* (*40*), and the chemokine *Cxcl2*, which has previously been shown to recruit myeloid-derived suppressor cells and drive immune suppression (*41*, *42*). The fact that these genes are only up-regulated upon IRF1 deletion and not deletion of IKKβ or IFN-γ blockade implies a specific role for IRF1 in their repression independently of NF-κB/IFN-γ signaling, this is certainly an observation that requires further investigation.

Several lines of evidence point to a hierarchical relationship between NF-κB and IRF1 activation in tumor-associated cDC1s. First, IRF1-dependent genes in cDC1s were not enriched for NF-κB regulatory elements, whereas NF-κB–dependent genes were enriched for IRF1-mediated regulation. Second, NF-κB inactivation consistently decreased *Irf1* mRNA expression by intratumoral cDC1s. Third, the kinetics of increased NF-κB activation correlated with the induction of *Irf1* mRNA by cDC1s upon treatment with tumor-conditioned medium (TCM) in vitro. Last, consistent with NF-κB–mediated regulation of IRF1 expression, the regulatory regions of the mouse and human *IRF1* genes contain 23 and 37 NF-κB binding sites, respectively (*43*). We used scRNA-seq data to decipher the trajectory of intratumoral cDC1 maturation, which revealed a transitional cell state enriched for IFN response pathways that preceded full maturation. This transitional cDC1 population increased upon NF-κB or IRF1 deletion, consistent with a role for NF-κB/IRF1 signaling in the IFN-dependent progression of cDC1 maturation. Accumulation of this IFN pathway–enriched transitional state in the absence NF-κB/IRF1 signaling implied that only a subset of IFN-responsive genes in cDC1s are required for antitumor immunity and that these genes are critically regulated by NF-κB and IRF1. This is consistent with a previous study that showed a selective role of IRF1 in expression of inflammatory but not antiviral genes during IFN responses (*35*). The enrichment of IFN pathways in cDC1s upon deletion of NF-κB/IRF1 may also reflect cross-regulation between IFN-γ– and type I IFN (IFN-I)–regulated pathways, i.e., the arrest of IFN-γ–mediated cDC1 maturation upon deletion of NF-κB or IRF1 may lead to a compensatory increase in cDC1 responses to IFN-I. Previous studies have shown that IFN-γ and IFN-I pathways can antagonize one another in certain contexts (*44*–*46*).

Among the genes regulated by NF-κB and IRF1 in intratumoral cDC1s, T cell chemokines were conspicuous, including *Ccl5*, *Ccl22*, *Cxcl9*, and *Cxcl10*. These chemokines appeared to be selectively expressed during cDC1 maturation. CXCL9 and CXCL10 were mostly expressed during the transitional cDC1 maturation state, associated with high enrichment for IFN response pathways, whereas CCL5 and CCL22 were selectively expressed in fully mature cDC1s. This was in keeping with the poor infiltration of CD8⁺ T cells in tumors upon conditional deletion of NF-κB or IRF1 signaling in cDC1s. Other NF-κB/IRF1–regulated genes in intratumoral cDC1s were related to antigen cross-presentation (*47*, *48*) and T cell activation (*29*, *31*, *49*). Therefore, activation of the NF-κB/IRF1 axis in intratumoral cDC1s likely promoted both the recruitment and activation of CD8⁺ T cells.

Although not addressed directly here, the migratory capacity of tumor-associated cDC1s is likely to be critical for control of tumor growth in the context of immunotherapy. The expression of genes required for cDC migration, namely, *Ccr7* and *Fscn1*, were up-regulated in mature intratumoral cDC1s (C1 and C2). We also analyzed the enrichment of published GSs from migratory cDCs across all intratumoral cDC1 clusters, which showed a selective enrichment in C1 and C2 (fig. S7O). These data suggest that intratumoral cDC1 maturation is associated with induction of a migratory gene program. Further studies are required to dissect the roles of NF-κB and IRF1 signaling in the migratory capacity of intratumoral cDC1s and the impact on antitumor immunity. Another unexplored perspective from this work is the instructive signal for NF-κB–mediated cDC1 maturation in tumors. Given the enrichment of IFN-I and IFN-γ response pathways during intratumoral cDC1 maturation,

the cyclic guanosine monophosphate-adenosine monophosphate (cGAMP)–stimulator of interferon genes (STING) pathway is an attractive candidate, which may be triggered by host DNA derived from dying cells. However, TNF signaling was also up-regulated during intratumoral cDC1 maturation, and TNF-α is known to synergize with IFN response pathways through induction of IRF1 in macrophages.

Our data describe an NF-κB/IRF1 axis that governs intratumoral cDC1 maturation and their ability to control tumor growth in a clinically relevant model of melanoma. We also analyzed TCGA data for human melanoma and found a correlation between the enrichment of NF-κB/IRF1–regulated genes associated with cDC1s and activated $CD8^+$ T cell genes, both of which indicated a superior clinical prognosis for patients. These analyses are based on enrichment of NF-κB/IRF1–dependent genes in the cDC1 GS and do not imply an exclusive expression of these genes in cDC1s. Athough, NF-κB, and more prominently IRF1, showed a high correlation with the cDC1 GS and their enrichment was positively associated with patient survival. This suggests that the role of NF-κB/IRF1 signaling in intratumoral cDC1 maturation may be conserved in human cancer and plays a critical role in limiting disease progression.

MATERIALS AND METHODS

Study design

The main aim of this study was to investigate the molecular mechanisms that govern the antitumoral functions of cDC1s. By using scRNA-seq and a mouse model of melanoma, we identified NF-κB and IFN pathways as molecular determinants of intratumoral cDC1 maturation. We generated transgenic mice to block NF-κB and IRF1 signaling specifically in cDC1s to study their impact on cDC1 maturation and antitumor immune responses. Last, we analyzed clinical data from TCGA databases to query the impact of NF-κB/IRF1 pathways in association with cDC1s and T cell activation GSs on clinical outcome in patients with cancer.

Mice

Mice were housed at Centre d'immunologie Marseille Luminy with water and food ad libitum and 12-hour/12-hour night/daylight cycle under specific pathogen–free conditions and handled in accordance with French and European directives. All animal experimentation was approved by the Direction Départementale des Services Vétérinaires des Bouches du Rhône. C57BL/6J mice were purchased from Janvier Labs. Experiments were performed with sex-matched littermate mice at 6 to 12 weeks of age. The following transgenic mouse strains were used in this study: *Xcr1*^{Cre} (*B6-Xcr1*^{tm1Ciphe}) (*27*), *Xcr1*$^{TEAL\text{-}Cre}$ (*B6-Xcr1*^{tm2Ciphe}) (*26*), *Ikbkb*$^{F/F}$ (*B6-Ikbkb*^{tm2Mka}) (*50*), *Irf1*$^{F/F}$ (*B6-Irf1*$^{tm1c(EUCOMM)Wtsi}$) (*51*) and *Cxcl9*$^{F/F}$ (*B6-Cxcl9*^{tm1Ciphe}) (this paper), and *Rosa26*$^{LSL\text{-}DTA}$ (*B6.129P2-Gt(ROSA)26*$^{Sortm1(DTA)Lky/J}$) (*28*). Additional details are provided in table S1.

Tumor cell cultures and injections

Mycoplasma-free YUMM1.7 (*21*) or YUMMER1.7 (*22*) was cultured at 37°C, 5% CO_2 in RPMI 1640 medium with 10% heat-inactivated fetal calf serum (Biochrom, Cambridge, UK), penicillin/streptomycin, and 50 mM β-mercaptoethanol. YUMM1.7 or YUMMER1.7 cultures were washed in phosphate-buffered saline (PBS; pH 7.4) and harvested with PBS containing 2 mM EDTA, for 2 min at 37°C, and then washed again in PBS. A total of 1×10^6 cells were injected subcutaneously in 100 μl of endotoxin-free PBS on the right flank of recipient mice. Tumor growth was measured using a digital caliper. Tumor volume stated in the figures was calculated as $L \times l^2$, considering the longest diameter (L) and its perpendicular (l) for each tumor.

Tissue processing for flow cytometry

Tumors were minced and digested in RPMI 1640, collagenase II (1 mg/ml) (Sigma-Aldrich), deoxyribonuclease I (50 μg/ml) (Roche), and 0.1% (w/v) bovine serum albumin (BSA) for 30 min at 37°C with 750-rpm agitation. Cell suspensions were subsequently passed through a 70-μm cell strainer (BD Biosciences) and collected by centrifugation.

Flow cytometry

Flow cytometric analyses and cell sorting were performed using LSR Fortessa X20 or LSR-2 flow cytometers and Aria cell sorter, respectively. Cells were preincubated with 2.4G2 antibody to block unspecific binding to Fc receptors in all stainings. Staining with antibodies (details provided in table S2) was performed in PBS, 2% fetal bovine serum, and 2 mM EDTA for 20 min at 4°C. For exclusion of dead cells, LIVE/DEAD Fixable Cell Stain kit (Invitrogen) was used in all experiments. H-Y–specific tetramers [$Smcy_{(738–746)}$/H-2Db and $Uty_{(243–254)}$/H-2Db] were provided from National Institutes of Health Tetramer Core Facility and coupled to streptavidin-allophycocyanin. Incubation with H-Y tetramers was carried out at 10 nM for 40 min at 4°C, before staining with antibodies. Data were analyzed using FlowJo (Tree Star Inc.).

Bone marrow–derived DCs

Bone marrow (BM)–derived DCs were generated as described (*51*). Briefly, BM cells were incubated with granulocyte-macrophage colony-stimulating factor (GM-CSF) (10 ng/ml; PeproTech, 315-03) and 1/10 FLT3L supernatant in RPMI 1640 medium with 10% heat-inactivated fetal calf serum (Biochrom, Cambridge, UK), penicillin/streptomycin, and 50 mM β-mercaptoethanol. BM cells were incubated in 10 ml of complete medium with FLT3L combined with GM-CSF for 9 days and subsequently replated with the same combination of cytokines and harvested at day 15. Treatment with TCM was carried out the last day before harvesting. TCM was produced by mincing YUMM1.7 tumor explants and incubating them at RPMI 1640 medium (50 mg/ml) with 10% heat-inactivated fetal calf serum, penicillin/streptomycin, and 50 mM β-mercaptoethanol for 24 hours at 37°C.

Western blot analysis

Cells were washed and harvested in ice-cold PBS, and pellets were lysed on ice in radioimmunoprecipitation assay buffer [150 mm NaCl, 1% Nonidet P-40, 0.5% sodium deoxycholate, 0.1% SDS, and 50 mm tris (pH 8.0)] containing a protease inhibitor cocktail (Sigma-Aldrich, P8340), 1 mM phenylmethylsulfonyl fluoride, 2 mM p-nitrophenyl phosphate, disodium salt (PNPP), 10 mM glycerol, 100 μM orthovanadate, and 1 mM dithiothreitol. After 1 hour of incubation on ice with frequent agitations, cell lysates were centrifuged at 12,000*g* for 10 min, the supernatants were collected, and the concentration of proteins was determined using the DC protein assay, according to the manufacturer's instructions (Bio-Rad Laboratories). Proteins (75 μg) from the various lysates were separated on 10 to 13% polyacrylamide slab gels (depending on the size of the protein to be analyzed) and transferred to polyvinylidene fluoride membranes. The membranes were blocked with 5% skimmed milk in PBS for 1 hour at room temperature and reacted for 16 hours at

4°C with the appropriate primary antibody (details provided in table S2). Primary and horseradish peroxidase–conjugated antibodies were applied in 3% BSA in PBS, containing 0.02% sodium azide. Incubations with secondary antibodies were for 1 hour at room temperature. Membranes were rinsed between incubations three times with PBS and 0.05% Tween 20. After the last wash, membranes were imaged using Amersham ECL Prime (GE Healthcare, RPN2232).

High-throughput gene expression analysis

Purification of total RNA from sorted cells was performed by using the RNeasy Plus Micro Kit (QIAGEN) and concentration was determined using the Quant-IT RiboGreen RNA assay kit (Thermo Fisher Scientific). Total RNA (2.5 ng) was used for first-strand complementary DNA (cDNA) synthesis with High Capacity cDNA Reverse Transcription Kit (Thermo Fisher Scientific) followed by a 15-cycle preamplification PCR of genes of interest using the Fluidigm PreAmp Master Mix (Fluidigm Europe B.V.) in accordance with the manufacturer's instructions. Samples were subsequently treated with exonuclease I (New England Biolabs) to remove unincorporated primers and diluted 1:5 in tris-EDTA buffer. High-throughput gene expression analysis was performed using the 96.96 or 48.48 dynamic arrays and BioMark HD system from Fluidigm in accordance with the manufacturer's instructions and standard settings. Exon-spanning primers to amply genes of interest were designed using Primer-BLAST (details provided in table S3). Obtained data were analyzed using the Real-Time PCR Analysis Software (Fluidigm), and resulting Ct (threshold cycle) values were normalized to *Actb* or *Ppia*. Heatmaps, *z* scores, and hierarchical clustering using the one minus Pearson correlation were generated using Morpheus (https://software.broadinstitute.org/morpheus/). Statistical analyses were performed by multiple unpaired *t* test with unadjusted *P* values.

Enrichment analyses

GSEA on bulk RNA-seq data was run to calculate normalized enrichment score (NES) using metric for ranking genes: Diff_of_classes and classic enrichment statistics. Enrichment analysis of scRNA-seq data was performed using the EnrichR tool (https://amp.pharm.mssm.edu/Enrichr/). Combined scores were calculated by multiplying the log of the *P* value computed with the Fisher's exact test by the *z* score computed by the correction to this test. DEGs were selected upon setting an arbitrary cutoff for significance at $P < 0.00001$ and false discovery rate (FDR)–adjusted $P < 0.25$. For the EnrichR analysis of the cluster markers from the WT dataset (Fig. 2), only positive markers with an adjusted $P < 0.05$ were considered. The hub nodes on EnrichR networks were generated following the tools as previously described (*52*, *53*).

Single-cell sorting and library preparation

Single cells were fluorescence-activated cell–sorted into ice-cold 96-well PCR plates (Thermo Fisher Scientific) containing 2-μl lysis mix per well. The lysis mix contained 0.5 μl of 0.4% (v/v) Triton X-100 (Sigma-Aldrich), 0.05 μl of RNaseOUT (40 U/μl; Thermo Fisher Scientific), 0.08 μl of 25 mM deoxyribose nucleotide triphosphate mix (Thermo Fisher Scientific), 0.5 μl of 10 μM (dT)30_Smarter primer (*54*), 0.05 μl of External RNA Controls Consortium (ERCC) spike-ins mix (0.5 pg/μl; Thermo Fisher Scientific), and 0.82 μl of PCR-grade H20 (QIAGEN). Oligonucleotides used to generate the scRNA-seq libraries are provided in table S4. The plates containing single cells in lysis mix were stored at −80°C until further processing for amplification and library preparation, according to previously published procedures (*55*). The resulting libraries were purified with 0.8× solid-phase reversible immobilization beads (AMPureXP, Beckman or CleanNGS, Proteigene). Libraries generated from multiple 96-well plates of single cells and carrying distinct i7 barcodes were pooled for sequencing on an Illumina NextSeq 550 platform, with High Output 75-cycle flow cells, targeting 5×10^5 reads per cell in paired-end single-index mode with the primers previously reported (*54*) and cycles Read1 (Read1_SP, 67 cycles), Read i7 (i7_SP, 8 cycles), and Read2 (Read2_SP, 16 cycles).

scRNA-seq data analysis

FB5P-seq

Raw fastq files were processed to generate single-cell UMI count matrices as described (*54*). Read alignment on the mouse reference genome (GRCm38.94 with ERCC92) was performed using Spliced Transcripts Alignment to a Reference (v2.5.3a). Digital gene expression data were extracted using Drop-Seq software (v1.12). The counts matrix was loaded to R (3.6.1) and Seurat (v3.1.5) (*56*) was used for downstream analyses in a similar way as in the study by Abbas *et al*. (*57*). First, we selected the genes that were expressed in at least five cells. Then, we excluded the cells that had less than 600 detected genes or more than 10% mitochondrial genes. We identified contaminants on the basis of two approaches: (i) performing connectivity map analysis (cmap) using homemade signatures and (ii) using FindMarkers functions in Seurat to identify the genes for characterizing the clusters. These two approaches allowed us to identify and remove five clusters (C4, C9, C10, C12, and C13; $n = 110$) as contaminants.

Analysis of scRNA-seq data

For Fig. 2 and fig. S2, we obtained 113 bona fide cDC1s. Gene expression is shown as log(normalized values). Afterward, principal components analysis (PCA) was performed using the highly variable genes. A shared nearest neighbor (SNN) graph was built using the four first principal components with the FindNeighbors function (dims = 1:4, k.param = 20). Clustering was then performed with a resolution of 1.3. For dimensionality reduction, we performed a UMAP using the RunUMAP function (n.neighbors = 7, spread = 1, min.dist = 2.5).

For Fig. 6 and fig. S6, we obtained 360 bona fide cDC1s. A SNN graph was built using the six first principal components. Clustering was performed with a resolution of 0.6. A UMAP was performed using the RunUMAP function (n.neighbors = 7, spread = 1, min.dist = 0.6). The DEGs were determined using the FindMarkers function (test.use = "bimod", min.pct = 0.5).

Heatmaps

Heatmaps based on z scores and hierarchical clustering using the one minus Pearson correlation were generated using Morpheus (https://software.broadinstitute.org/morpheus/).

Analysis of scRNA-seq data from LUAD

scRNA-seq data of DCs from the lungs of WT tumor-naïve and tumor-bearing mice were downloaded from GEO using accession codes GSM3832735 and GSM3832737 (*15*). The count matrix was loaded to R and Seurat as described above. We used the same parameters and the same strategy as described above to exclude contaminating cells. From 4695 starting cells, we retained 1418 cells identified as cDC1.

Alignment of clusters from melanoma and LUAD datasets

Marker genes of clusters for each dataset were extracted separately, using the FindMarkers function of Seurat and the "bimod" parameter.

We then computed the JIs between each cluster of one dataset with any other cluster of the other dataset, as already published (*57*). The JI measures similarity between finite sample sets and is defined as the size of the intersection divided by the size of the union of the sample sets: $J(A, B) = |A \cap B| / |A \cup B|$. The JI matrix was then used to generate a heatmap.

BubbleMap

High-throughput GSEA was performed to assess the enrichment of selected transcriptomic signatures across clusters of the scRNA-seq data, using BubbleMap from the BubbleGUM (v1.3.19) suite (*58*), with the default parameters except the following: number of permutations: 6000, max gene set size = 5000, min gene set size = 10. We used the Hallmark and KEGG gene set collections (v7.0) from the MSigDB (*53*). We also used gene sets of genes up-regulated (Mat ON/Core UP) and down-regulated (Mat OFF/Core DN) during DC maturation (*29*, *31*).

Pseudotemporal analysis

We used Monocle (v3) to investigate cell trajectories and the dynamics of gene expression within these trajectories. The input cells and genes were selected using Seurat. We first clustered and projected the cells onto a low-dimensional space (UMAP) calculated by Seurat. Last, Monocle resolved the activation trajectories and calculated along them the pseudotime for each cell using monocle functions reduce_dimensions (max_components = 3; reduction_method = "UMAP"; preprocess_method = "PCA"; umap.min_dist = 0.8; umap.n_neighbors = 10) and cluster_cells (resolution = 2^{-2}; reduction_method = "UMAP"; k = 15; num_iter = 2;).

Computational analysis of cancer patient data

Datasets for all the patients with melanoma whose tumors were profiled with RNA-seq were downloaded from the GDC Data Portal (https://portal.gdc.cancer.gov/). This resulted in a cohort of 468 patients, all coming from TCGA-SKCM project. The expression values, FPKM (fragments per kilobase of exon model per million reads mapped), for each of the selected genes across these patients were retrieved, and GS scores were calculated for each of them. These scores are defined as the average expression of the genes forming the defined GS. Subcohorts were identified using a given GS (e.g., patients with cDC1-enriched tumors or those in the top quartile of a given GS). The annotated survivals of all the patients in the identified subcohorts were retrieved from the GDC Data Portal to draw the corresponding Kaplan-Meier survival plots. Heatmaps, *z* scores, and hierarchical clustering using the one minus Pearson correlation were generated using Morpheus (https://software.broadinstitute.org/morpheus/). GS analyses for LUAD database from TCGA were generated using GEPIA2 (http://gepia2.cancer-pku.cn/) (*59*).

Statistical analysis

Where indicated, *P* values were calculated using either two-way analysis of variance (ANOVA) followed by Sidak's multiple comparison test or Mann-Whitney test, where appropriate, using GraphPad prism software. Significance threshold for Fisher's exact test is 0.1. $*P < 0.05$; $**P < 0.01$; $***P < 0.001$; $****P < 0.0001$.

SUPPLEMENTARY MATERIALS

immunology.sciencemag.org/cgi/content/full/6/61/eabg3570/DC1
Figs. S1 to S10
Tables S1 to S4
Data files S1 and S2

View/request a protocol for this paper from *Bio-protocol*.

REFERENCES AND NOTES

1. S. Spranger, D. Dai, B. Horton, T. F. Gajewski, Tumor-residing Batf3 dendritic cells are required for effector T cell trafficking and adoptive T cell therapy. *Cancer Cell* **31**, 711–723.e4 (2017).
2. J. Li, K. T. Byrne, F. Yan, T. Yamazoe, Z. Chen, T. Baslan, L. P. Richman, J. H. Lin, Y. H. Sun, A. J. Rech, D. Balli, C. A. Hay, Y. Sela, A. J. Merrell, S. M. Liudahl, N. Gordon, R. J. Norgard, S. Yuan, S. Yu, T. Chao, S. Ye, T. S. K. Eisinger-Mathason, R. B. Faryabi, J. W. Tobias, S. W. Lowe, L. M. Coussens, E. J. Wherry, R. H. Vonderheide, B. Z. Stanger, Tumor cell-intrinsic factors underlie heterogeneity of immune cell infiltration and response to immunotherapy. *Immunity* **49**, 178–193.e7 (2018).
3. T. Mao, E. Song, A. Iwasaki, PD-1 blockade-driven anti-tumor $CD8^+$ T cell immunity requires $XCR1^+$ dendritic cells. *bioRxiv* 10.1101/2020.04.28.066639 , (2020).
4. J. C. Cancel, K. Crozat, M. Dalod, R. Mattiuz, Are conventional type 1 dendritic cells critical for protective antitumor immunity and how? *Front. Immunol.* **10**, 9 (2019).
5. K. Crozat, R. Guiton, V. Contreras, V. Feuillet, C. A. Dutertre, E. Ventre, T.-P. V. Manh, T. Baranek, A. K. Storset, J. Marvel, P. Boudinot, A. Hosmalin, I. Schwartz-Cornil, M. Dalod, The XC chemokine receptor 1 is a conserved selective marker of mammalian cells homologous to mouse CD8α+ dendritic cells. *J. Exp. Med.* **207**, 1283–1292 (2010).
6. A. Bachem, S. Güttler, E. Hartung, F. Ebstein, M. Schaefer, A. Tannert, A. Salama, K. Movassaghi, C. Opitz, H. W. Mages, V. Henn, P. M. Kloetzel, S. Gurka, R. A. Kroczek, Superior antigen cross-presentation and XCR1 expression define human $CD11c^+CD141^+$ cells as homologues of mouse $CD8^+$ dendritic cells. *J. Exp. Med.* **207**, 1273–1281 (2010).
7. D. J. Theisen, J. T. Davidson, C. G. Briseño, M. Gargaro, E. J. Lauron, Q. Wang, P. Desai, V. Durai, P. Bagadia, J. R. Brickner, W. L. Beatty, H. W. Virgin, W. E. Gillanders, N. Mosammaparast, M. S. Diamond, L. D. Sibley, W. Yokoyama, R. D. Schreiber, T. L. Murphy, K. M. Murphy, WDFY4 is required for cross-presentation in response to viral and tumor antigens. *Science* **362**, 694–699 (2018).
8. T. P. V. Manh, N. Bertho, A. Hosmalin, I. Schwartz-Cornil, M. Dalod, Investigating evolutionary conservation of dendritic cell subset identity and functions. *Front. Immunol.* **6**, 260 (2015).
9. D. J. Theisen, S. T. Ferris, C. G. Briseño, N. Kretzer, A. Iwata, K. M. Murphy, T. L. Murphy, *Batf3*-Dependent genes control tumor rejection induced by dendritic cells independently of cross-presentation. *Cancer Immunol. Res.* **7**, 29–39 (2019).
10. S. T. Ferris, V. Durai, R. Wu, D. J. Theisen, J. P. Ward, M. D. Bern, J. T. Davidson, P. Bagadia, T. Liu, C. G. Briseño, L. Li, W. E. Gillanders, G. F. Wu, W. M. Yokoyama, T. L. Murphy, R. D. Schreiber, K. M. Murphy, cDC1 prime and are licensed by $CD4^+$ T cells to induce anti-tumour immunity. *Nature* **584**, 624–629 (2020).
11. H. Salmon, J. Idoyaga, A. Rahman, M. Leboeuf, R. Remark, S. Jordan, M. Casanova-Acebes, M. Khudoynazarova, J. Agudo, N. Tung, S. Chakarov, C. Rivera, B. Hogstad, M. Bosenberg, D. Hashimoto, S. Gnjatic, N. Bhardwaj, A. K. Palucka, B. D. Brown, J. Brody, F. Ginhoux, M. Merad, Expansion and activation of CD103+ dendritic cell progenitors at the tumor site enhances tumor responses to therapeutic PD-L1 and BRAF inhibition. *Immunity* **44**, 924–938 (2016).
12. A. R. Sánchez-Paulete, F. J. Cueto, M. Martínez-López, S. Labiano, A. Morales-Kastresana, M. E. Rodríguez-Ruiz, M. Jure-Kunkel, A. Azpilikueta, M. A. Aznar, J. I. Quetglas, D. Sancho, I. Melero, Cancer immunotherapy with immunomodulatory anti-CD137 and anti–PD-1 monoclonal antibodies requires BATF3-dependent dendritic cells. *Cancer Discov.* **6**, 71–79 (2016).
13. K. C. Barry, J. Hsu, M. L. Broz, F. J. Cueto, M. Binnewies, A. J. Combes, A. E. Nelson, K. Loo, R. Kumar, M. D. Rosenblum, M. D. Alvarado, D. M. Wolf, D. Bogunovic, N. Bhardwaj, A. I. Daud, P. K. Ha, W. R. Ryan, J. L. Pollack, B. Samad, S. Asthana, V. Chan, M. F. Krummel, A natural killer–dendritic cell axis defines checkpoint therapy–responsive tumor microenvironments. *Nat. Med.* **24**, 1178–1191 (2018).
14. K. Hildner, B. T. Edelson, W. E. Purtha, M. Diamond, H. Matsushita, M. Kohyama, B. Calderon, B. U. Schraml, E. R. Unanue, M. S. Diamond, R. D. Schreiber, T. L. Murphy, K. M. Murphy, Batf3 deficiency reveals a critical role for $CD8\alpha^+$ dendritic cells in cytotoxic T cell immunity. *Science* **322**, 1097–1100 (2008).
15. B. Maier, A. M. Leader, S. T. Chen, N. Tung, C. Chang, J. LeBerichel, A. Chudnovskiy, S. Maskey, L. Walker, J. P. Finnigan, M. E. Kirkling, B. Reizis, S. Ghosh, N. R. D'Amore, N. Bhardwaj, C. V. Rothlin, A. Wolf, R. Flores, T. Marron, A. H. Rahman, E. Kenigsberg, B. D. Brown, M. Merad, A conserved dendritic-cell regulatory program limits antitumour immunity. *Nature* **580**, 257–262 (2020).
16. C. S. Garris, S. P. Arlauckas, R. H. Kohler, M. P. Trefny, S. Garren, C. Piot, C. Engblom, C. Pfirschke, M. Siwicki, J. Gungabeesoon, G. J. Freeman, S. E. Warren, S. F. Ong, E. Browning, C. G. Twitty, R. H. Pierce, M. H. Le, A. P. Algazi, A. I. Daud, S. I. Pai, A. Zippelius, R. Weissleder, M. J. Pittet, Successful anti-PD-1 cancer immunotherapy requires T cell-dendritic cell crosstalk involving the cytokines IFN-γ and IL-12. *Immunity* **49**, 1148–1161.e7 (2018).
17. H. Tang, Y. Wang, L. K. Chlewicki, Y. Zhang, J. Guo, W. Liang, J. Wang, X. Wang, Y.-X. Fu, Facilitating T cell infiltration in tumor microenvironment overcomes resistance to PD-L1 blockade. *Cancer Cell* **29**, 285–296 (2016).

18. D. Chowell, L. G. T. Morris, C. M. Grigg, J. K. Weber, R. M. Samstein, V. Makarov, F. Kuo, S. M. Kendall, D. Requena, N. Riaz, B. Greenbaum, J. Carroll, E. Garon, D. M. Hyman, A. Zehir, D. Solit, M. Berger, R. Zhou, N. A. Rizvi, T. A. Chan, Patient HLA class I genotype influences cancer response to checkpoint blockade immunotherapy. *Science* **359**, 582–587 (2018).
19. J. M. Zaretsky, A. Garcia-Diaz, D. S. Shin, H. Escuin-Ordinas, W. Hugo, S. Hu-Lieskovan, D. Y. Torrejon, G. Abril-Rodriguez, S. Sandoval, L. Barthly, J. Saco, B. Homet Moreno, R. Mezzadra, B. Chmielowski, K. Ruchalski, I. P. Shintaku, P. J. Sanchez, C. Puig-Saus, G. Cherry, E. Seja, X. Kong, J. Pang, B. Berent-Maoz, B. Comin-Anduix, T. G. Graeber, P. C. Tumeh, T. N. M. Schumacher, R. S. Lo, A. Ribas, Mutations associated with acquired resistance to PD-1 blockade in Melanoma. *N. Engl. J. Med.* **375**, 819–829 (2016).
20. T. Jiang, T. Shi, H. Zhang, J. Hu, Y. Song, J. Wei, S. Ren, C. Zhou, Tumor neoantigens: From basic research to clinical applications. *J. Hematol. Oncol.* **12**, 93 (2019).
21. K. Meeth, J. X. Wang, G. Micevic, W. Damsky, M. W. Bosenberg, The YUMM lines: A series of congenic mouse melanoma cell lines with defined genetic alterations. *Pigment Cell Melanoma Res.* **29**, 590–597 (2016).
22. J. Wang, C. J. Perry, K. Meeth, D. Thakral, W. Damsky, G. Micevic, S. Kaech, K. Blenman, M. Bosenberg, UV-induced somatic mutations elicit a functional T cell response in the YUMMER1.7 mouse melanoma model. *Pigment Cell Melanoma Res.* **30**, 428–435 (2017).
23. R. Popli, B. Sahaf, H. Nakasone, J. Y. Y. Lee, D. B. Miklos, Clinical impact of H-Y alloimmunity. *Immunol. Res.* **58**, 249–258 (2014).
24. M. A. Ataide, K. Komander, K. Knöpper, A. E. Peters, H. Wu, S. Eickhoff, T. Gogishvili, J. Weber, A. Grafen, A. Kallies, N. Garbi, H. Einsele, M. Hudecek, G. Gasteiger, M. Hölzel, M. Vaeth, W. Kastenmüller, BATF3 programs $CD8^+$ T cell memory. *Nat. Immunol.* **21**, 1397–1407 (2020).
25. Z. Qiu, C. Khairallah, G. Romanov, B. S. Sheridan, Cutting Edge: *Batf3* expression by CD8 T cells critically regulates the development of memory populations. *J. Immunol.* **205**, 901–906 (2020).
26. C. Wohn, V. Le Guen, O. Voluzan, F. Fiore, S. Henri, B. Malissen, Absence of MHC class II on cDC1 dendritic cells triggers fatal autoimmunity to a cross-presented self-antigen. *Sci. Immunol.* **5**, eaba1896 (2020).
27. R. Mattiuz, C. Wohn, S. Ghilas, M. Ambrosini, Y. O. Alexandre, C. Sanchez, A. Fries, T. P. V. Manh, B. Malissen, M. Dalod, K. Crozat, Novel cre-expressing mouse strains permitting to selectively track and edit type 1 conventional dendritic cells facilitate disentangling their complexity in vivo. *Front. Immunol.* **9**, 2805 (2018).
28. D. Voehringer, H.-E. Liang, R. M. Locksley, Homeostasis and effector function of lymphopenia-induced "memory-like" T cells in constitutively T cell-depleted mice. *J. Immunol.* **180**, 4742–4753 (2008).
29. T. P. V. Manh, Y. Alexandre, T. Baranek, K. Crozat, M. Dalod, Plasmacytoid, conventional, and monocyte-derived dendritic cells undergo a profound and convergent genetic reprogramming during their maturation. *Eur. J. Immunol.* **43**, 1706–1715 (2013).
30. M. Baratin, C. Foray, O. Demaria, M. Habbeddine, E. Pollet, J. Maurizio, C. Verthuy, S. Davanture, H. Azukizawa, A. Flores-Langarica, M. Dalod, T. Lawrence, Homeostatic NF-κB signaling in steady-state migratory dendritic cells regulates immune homeostasis and tolerance. *Immunity* **42**, 627–639 (2015).
31. L. Ardouin, H. Luche, R. Chelbi, S. Carpentier, A. Shawket, F. Montanana Sanchis, C. Santa Maria, P. Grenot, Y. Alexandre, C. Grégoire, A. Fries, T.-P. V. Manh, S. Tamoutounour, K. Crozat, E. Tomasello, A. Jorquera, E. Fossum, B. Bogen, H. Azukizawa, M. Bajenoff, S. Henri, M. Dalod, B. Malissen, Broad and largely concordant molecular changes characterize tolerogenic and immunogenic dendritic cell maturation in Thymus and periphery. *Immunity* **45**, 305–318 (2016).
32. M. Singer, C. Wang, L. Cong, N. D. Marjanovic, M. S. Kowalczyk, H. Zhang, J. Nyman, K. Sakuishi, S. Kurtulus, D. Gennert, J. Xia, J. Y. H. Kwon, J. Nevin, R. H. Herbst, I. Yanai, O. Rozenblatt-Rosen, V. K. Kuchroo, A. Regev, A. C. Anderson, A distinct gene module for dysfunction uncoupled from activation in tumor-infiltrating T cells. *Cell* **166**, 1500–1511.e9 (2016).
33. Y. O. Alexandre, S. Ghilas, C. Sanchez, A. Le Bon, K. Crozat, M. Dalod, XCR1+ dendritic cells promote memory CD8+ T cell recall upon secondary infections with Listeria monocytogenes or certain viruses. *J. Exp. Med.* **213**, 75–92 (2016).
34. M. E. Mikucki, D. T. Fisher, J. Matsuzaki, J. J. Skitzki, N. B. Gaulin, J. B. Muhitch, A. W. Ku, J. G. Frelinger, K. Odunsi, T. F. Gajewski, A. D. Luster, S. S. Evans, Non-redundant requirement for CXCR3 signalling during tumoricidal T-cell trafficking across tumour vascular checkpoints. *Nat. Commun.* **6**, 7458 (2015).
35. A. Forero, S. Ozarkar, H. Li, C. H. Lee, E. A. Hemann, M. S. Nadjsombati, M. R. Hendricks, L. So, R. Green, C. N. Roy, S. N. Sarkar, J. von Moltke, S. K. Anderson, M. Gale Jr., R. Savan, Differential activation of the transcription factor IRF1 underlies the distinct immune responses elicited by type I and type III interferons. *Immunity* **51**, 451–464.e6 (2019).
36. C. Trapnell, D. Cacchiarelli, J. Grimsby, P. Pokharel, S. Li, M. Morse, N. J. Lennon, K. J. Livak, T. S. Mikkelsen, J. L. Rinn, The dynamics and regulators of cell fate decisions are revealed by pseudotemporal ordering of single cells. *Nat. Biotechnol.* **32**, 381–386 (2014).
37. J. P. Böttcher, E. Bonavita, P. Chakravarty, H. Blees, M. Cabeza-Cabrerizo, S. Sammicheli, N. C. Rogers, E. Sahai, S. Zelenay, C. Reis e Sousa, NK cells stimulate recruitment of cDC1 into the tumor microenvironment promoting cancer immune control. *Cell* **172**, 1022–1037.e14 (2018).
38. H. Yoshida, C. A. Hunter, The Immunobiology of Interleukin-27. *Annu. Rev. Immunol.* **33**, 417–443 (2015).
39. B. Carow, M. E. Rottenberg, SOCS3, a major regulator of infection and inflammation. *Front. Immunol.* **5**, 58 (2014).
40. J. C. Anania, A. M. Chenoweth, B. D. Wines, P. MarkHogarth, The human FcγRII (CD32) family of leukocyte FCR in health and disease. *Front. Immunol.* **10**, 464 (2019).
41. H. Zhang, Y. L. Ye, M. X. Li, S. B. Ye, W. R. Huang, T. T. Cai, J. He, J. Y. Peng, T. H. Duan, J. Cui, X. S. Zhang, F. J. Zhou, R. F. Wang, J. Li, CXCL2/MIF-CXCR2 signaling promotes the recruitment of myeloid-derived suppressor cells and is correlated with prognosis in bladder cancer. *Oncogene* **36**, 2095–2104 (2017).
42. H. Shi, X. Han, Y. Sun, C. Shang, M. Wei, X. Ba, X. Zeng, Chemokine (C-X-C motif) ligand 1 and CXCL 2 produced by tumor promote the generation of monocytic myeloid-derived suppressor cells. *Cancer Sci.* **109**, 3826–3839 (2018).
43. M. Iwanaszko, M. Kimmel, NF-κB and IRF pathways: Cross-regulation on target genes promoter level. *BMC Genomics* **16**, 307 (2015).
44. L. P. Cousens, J. S. Orange, H. C. Su, C. A. Biron, Interferon-α/β inhibition of interleukin 12 and interferon-γ production in vitro and endogenously during viral infection. *Proc. Natl. Acad. Sci. U.S.A.* **94**, 634–639 (1997).
45. W. J. Crisler, L. L. Lenz, Crosstalk between type I and II interferons in regulation of myeloid cell responses during bacterial infection. *Curr. Opin. Immunol.* **54**, 35–41 (2018).
46. S. Iwata, Y. Mikami, H.-W. Sun, S. R. Brooks, D. Jankovic, K. Hirahara, A. Onodera, H.-Y. Shih, T. Kawabe, K. Jiang, T. Nakayama, A. Sher, J. J. O'Shea, F. P. Davis, Y. Kanno, The transcription factor T-bet limits amplification of Type I IFN transcriptome and circuitry in T helper 1 cells. *Immunity* **46**, 983–991.e4 (2017).
47. M. Weimershaus, S. Maschalidi, F. Sepulveda, B. Manoury, P. van Endert, L. Saveanu, Conventional dendritic cells require IRAP-Rab14 endosomes for efficient cross-presentation. *J. Immunol.* **188**, 1840–1846 (2012).
48. J. M. Blander, Regulation of the cell biology of antigen cross-presentation. *Annu. Rev. Immunol.* **36**, 717–753 (2018).
49. Z. Chen, Z. Ji, S. F. Ngiow, S. Manne, Z. Cai, A. C. Huang, J. Johnson, R. P. Staupe, B. Bengsch, C. Xu, S. Yu, M. Kurachi, R. S. Herati, L. A. Vella, A. E. Baxter, J. E. Wu, O. Khan, J.-C. Beltra, J. R. Giles, E. Stelekati, L. M. McLane, C. W. Lau, X. Yang, S. L. Berger, G. Vahedi, H. Ji, E. J. Wherry, TCF-1-centered transcriptional network drives an effector versus exhausted CD8 T cell-fate decision. *Immunity* **51**, 840–855.e5 (2019).
50. J. M. Park, F. R. Greten, Z. W. Li, M. Karin, Macrophage apoptosis by anthrax lethal factor through p38 MAP kinase inhibition. *Science* **297**, 2048–2051 (2002).
51. C. N. Jondle, K. E. Johnson, A. A. Uitenbroek, P. A. Sylvester, C. Nguyen, W. Cui, V. L. Tarakanova, B cell-intrinsic expression of interferon regulatory factor 1 supports chronic murine Gammaherpesvirus 68 infection. *J. Virol.* **94**, e00399-20 (2020).
52. M. V. Kuleshov, M. R. Jones, A. D. Rouillard, N. F. Fernandez, Q. Duan, Z. Wang, S. Koplev, S. L. Jenkins, K. M. Jagodnik, A. Lachmann, M. G. McDermott, C. D. Monteiro, G. W. Gundersen, A. Ma'ayan, Enrichr: A comprehensive gene set enrichment analysis web server 2016 update. *Nucleic Acids Res.* **44**, W90–W97 (2016).
53. E. Y. Chen, C. M. Tan, Y. Kou, Q. Duan, Z. Wang, G. V. Meirelles, N. R. Clark, A. Ma'ayan, Enrichr: Interactive and collaborative HTML5 gene list enrichment analysis tool. *BMC Bioinformatics* **14**, 128 (2013).
54. N. Attaf, I. Cervera-Marzal, C. Dong, L. Gil, A. Renand, L. Spinelli, P. Milpied, Corrigendum: FB5P-seq: FACS-based 5-prime end single-cell RNA-seq for integrative analysis of transcriptome and antigen receptor repertoire in B and T cells. *Front. Immunol.* **11**, 2047 (2020).
55. C. T. Mayer, P. Ghorbani, A. Nandan, M. Dudek, C. Arnold-Schrauf, C. Hesse, L. Berod, P. Stüve, F. Puttur, M. Merad, T. Sparwasser, Selective and efficient generation of functional Batf3-dependent $CD103^+$ dendritic cells from mouse bone marrow. *Blood* **124**, 3081–3091 (2014).
56. A. Butler, P. Hoffman, P. Smibert, E. Papalexi, R. Satija, Integrating single-cell transcriptomic data across different conditions, technologies, and species. *Nat. Biotechnol.* **36**, 411–420 (2018).
57. A. Abbas, T. P. V. Manh, M. Valente, N. Collinet, N. Attaf, C. Dong, K. Naciri, R. Chelbi, G. Brelurut, I. Cervera-Marzal, B. Rauwel, J. L. Davignon, G. Bessou, M. Thomas-Chollier, D. Thieffry, A.-C. Villani, P. Milpied, M. Dalod, E. Tomasello, The activation trajectory of plasmacytoid dendritic cells in vivo during a viral infection. *Nat. Immunol.* **21**, 983–997 (2020).
58. L. Spinelli, S. Carpentier, F. Montañana Sanchis, M. Dalod, T.-P. V. Manh, BubbleGUM: Automatic extraction of phenotype molecular signatures and comprehensive visualization of multiple gene set enrichment analyses. *BMC Genomics* **16**, 814 (2015).
59. Z. Tang, B. Kang, C. Li, T. Chen, Z. Zhang, GEPIA2: An enhanced web server for large-scale expression profiling and interactive analysis. *Nucleic Acids Res.* **47**, W556–W560 (2019).

Acknowledgments: We thank A. Baranska for operational help in flow cytometry and sample preparation for scRNA-seq. We thank the CIML bioinformatics, cytometry, and histology platforms for technical and methodological support. **Funding:** This work was supported by institutional funding from the French National Institute of Health and Medical Research (INSERM), Centre National de la Recherche Scientifique (CNRS), and Aix-Marseille-Universite (AMU) and by grants to T.L. from the French Ligue Nationale Contre le Cancer (LNCC Equipe Labellisee EL2016-3) and Institut National du Cancer (INCa; PLBIO13-244), to K.C. from ARC (PJA20181207726), and to M.D. from INCa (PLBIO 2018-152). G.G. was funded by fellowships from LNCC and Marie-Curie actions IEF-Horizon2020 (REA grant agreement no. 702933). The project leading to this publication has received funding from the «Investissements d'Avenir» French Government program managed by the French National Research Agency (ANR-16-CONV-0001) and from Excellence Initiative of Aix-Marseille University-A*MIDEX, including a CENTURI PhD fellowship to A.S.C. **Author contributions:** G.G. performed most of the experiments and analyses, provided funding support, and cowrote the manuscript. T.P.V.M. supervised scRNA-seq analyses and performed BubbleGum analyses. A.S.C. performed scRNA-seq data analyses. E.B. performed the experiments characterizing immunogenicity of YUMM1.7 models. C.V. maintained transgenic mouse strains. K.C. generated and characterized *Xcr1*^{DTA}, *Cxcl9*$^{\Delta Xcr1}$, and *Cxcl9*$^{\Delta/\Delta}$ mice. N.A.-A. established YUMM1.7 models and their analyses and supervised YUMM1.7 immunogenicity experiments. P.J.B. performed the computational analyses of TCGA datasets. N.A. assisted with FB5P-seq library preparation. C.D. performed the primary bioinformatics analysis of FB5P-seq data. P.M. provided technical support and advice for the FB5P-seq strategy. B.M. provided access to *Xcr1-iCre* mice before their publication. M.D. supervised the studies and cowrote the manuscript. T.L. conceived and supervised the studies, provided funding support, and cowrote the manuscript. **Competing interests:** The authors declare that they have no competing interests. **Data and materials availability:** The GEO accession numbers for bulk and scRNA-seq data are GSE174089 and GSE171870, respectively. All other data needed to evaluate the conclusions of the paper are present in the paper or the Supplementary Materials. Transgenic mice are available under an MTA, and requests for access should be directed to the corresponding author.

Submitted 29 December 2020
Accepted 2 June 2021
Published 9 July 2021
10.1126/sciimmunol.abg3570

Citation: G. Ghislat, A. S. Cheema, E. Baudoin, C. Verthuy, P. J. Ballester, K. Crozat, N. Attaf, C. Dong, P. Milpied, B. Malissen, N. Auphan-Anezin, T. P. V. Manh, M. Dalod, T. Lawrence, NF-κB–dependent IRF1 activation programs cDC1 dendritic cells to drive antitumor immunity. *Sci. Immunol.* **6**, eabg3570 (2021